PLAXIS

SANISAND-MS UDSM

PLAXIS 3D 2023.2

Last updated: August, 2023

Seequent, The Bentley Subsurface Company

Table of Contents

1.

Introduction

For the last decades, increasing demand for renewable energy sources has stimulated immense advances in the construction of wind farms to enhance the production of green wind energies. Nowadays, new technologies allow for the installation of larger and more powerful wind turbines in more challenging environments. For example, in the North Sea, the turbine height has increased from 80 m in 2007 to 200 m in 2023. These larger structures require thereby more rational analysis and design of deeper and larger foundations, which may consist of a considerable part of the total installation cost (19-22 %, according to Houlsby, 2016).

The offshore wind turbine foundations are typically subjected to cyclic load scenarios characterized by both high amplitude loads during strong storms capable of mobilising their Ultimate Limit State (ULS), and small amplitude cyclic loads during their service life caused by wind, sea waves, streams, besides inertial loads. Especially for monopile foundations, i.e., foundations on a single pile with large diameter and small aspect ratio (embedment to diameter ratio, L/D), these small-amplitude lateral loads result in overturning moments and accumulation of tilting (Figure 1-1) that may eventually compromise the turbine strength, or the structure's fatigue life (LeBlanc et al., 2010). The prediction of the effects of cyclic load history on the response of the system is a complex task due to the strongly non-linear mechanical response of the soil (Abadie et al., 2023) and the computation effort required to simulate an extremely high number of cycles representative for the typical 25 years of service lives of wind turbines.

Many research studies are currently investigating how to evaluate the permanent rotation of the monopiles foundations. Simplified approaches span from semi-empirical models to 0D (Abadie et al., 2017; Houlsby et al., 2017; Abadie et al., 2023) models where the foundation is lumped in a macro element model or 1D models with degraded p-y curves (API 2000) or cyclic springs (Beuckelaers, 2017). In this context, 3DFEM numerical models using adequate soil constitutive laws are valuable to enhance the understanding and prediction of the geotechnical mechanisms occurring during the foundations' life cycle and to serve as a benchmark for the calibration, development, and verification of different design methods. A crucial component consists in modelling the mechanical behaviour of sands under thousands of repeated loads (high-cyclic conditions).

SANISAND-MS (Liu et al., 2019) is a bounding surface plasticity model developed to improve the simulation of the high-cyclic ratcheting of sands. As shown in Figure 1-2, under drained cyclic conditions (particularly under non-symmetric loading cycles), sands tend to accumulate progressively permanent strains – a phenomenon known as ratcheting –, most usually at a decreasing rate. Classic bounding surface models formulated for sands have limited capabilities in predicting the drained high cyclic ratcheting (Corti et al., 2016; Liu et al., 2019). The memory surface incorporated in SANISAND-MS has proven to be a key ingredient for capturing the fabric-related effects on the accumulation of permanent strains measured in high-cyclic laboratory tests (Liu et al., 2019, Liu and Pisanò, 2019). Recent studies (Liu et al., 2022a, Liu et al 2022b, Li et al., 2023) are showing the capabilities of the constitutive framework to predict the tilting of monopile foundations. Moreover, SANISAND-MS is implemented as a User Defined Soil Model (UDSM) in PLAXIS 3D, which allows the modelling of soil structure interaction under a high number of cycles and realistic loading and ground conditions with still-high-but-acceptable computational resources thanks to a robust finite element framework. As such, PLAXIS SANISAND-MS is particularly suitable for the assessment of the cyclic response of offshore structures. The potential range of applications extends to other engineering problems where the prediction strain accumulation under drained cyclic conditions is relevant. For example, the model could be used to evaluate differential settlements of foundations, induced by deterministic or random cyclic conditions due to high-speed traffic loads, vibrating machines, vibrating methos used to install piles as reported by Wicthmann (2005).

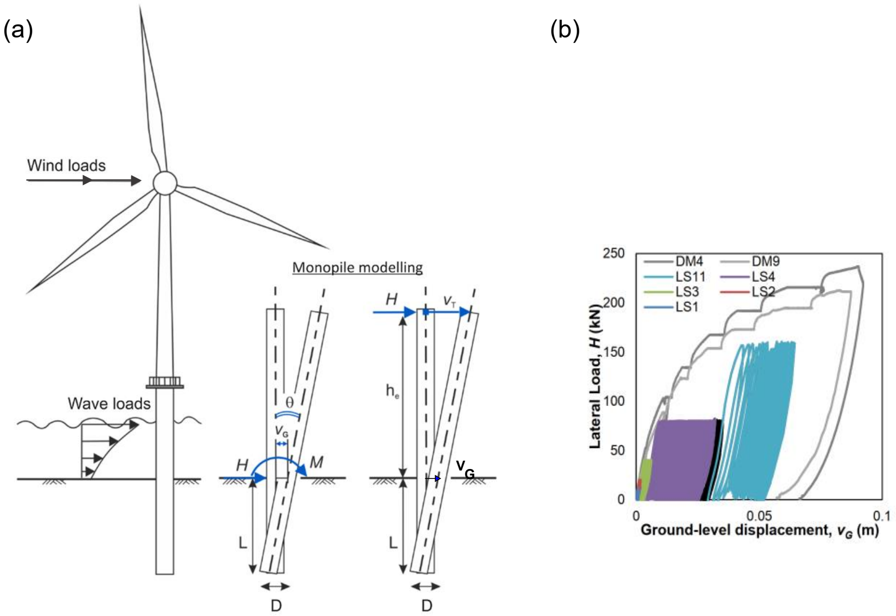

Figure 1-1 (a) Schematic illustration of an offshore wind turbine supported by a monopile foundation. Tilting and lateral displacement of the monopile caused by the lateral forces and the overturning moment. (After Abadie et al., 2023) (b) Experimental load-displacement response of laterally loaded piles. The cyclic test results show the permanent displacements at the ground surface (Byron et al., 2020)

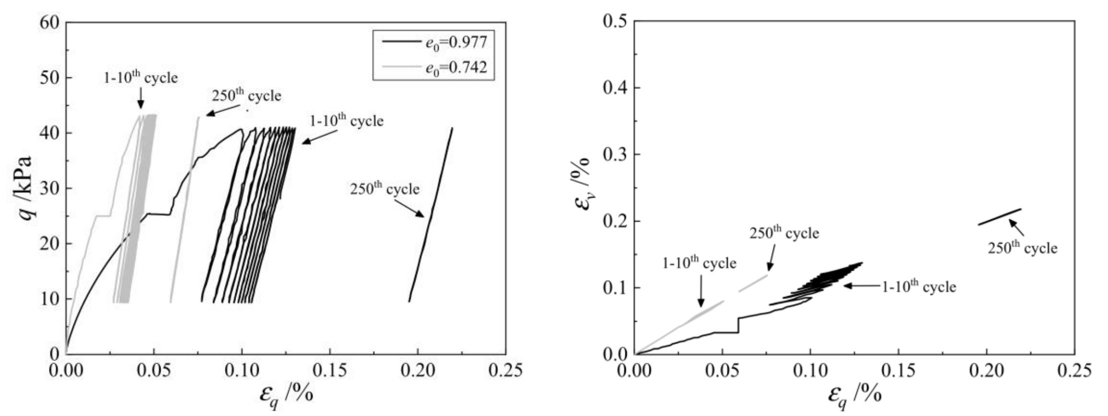

Figure 1-2 Results of drained cyclic triaxial tests on the Hostun sand (Escribano, 2014). In the stress-controlled (constant amplitude) asymmetrical test, both deviatoric and volumetric strain accumulation, with decreasing rate, is observed

2.

Model formulation

2.1 Conceptual framework and background

SANISAND-MS (Liu et al., 2019) is a constitutive model primarily developed to predict the high-cyclic stress-strain response of sands under drained conditions. The model framework is based on the well-known SANISAND04 model (Dafalias and Manzari, 2004), where the concept of a Memory Surface (MS) replaces the fabric dilatancy tensor included in its predecessor SANISAND04. Following the work of Corti et al. (2016), Liu et al. (2019) utilise the MS concept to keep track of the loading history and to account for fabric-related effects on the cyclic ratcheting of sands.

Some key features of the SANISANS-MS formulation, which complies with the bounding surface and critical state theories are presented first in the triaxial compression conditions. The general definitions in the multiaxial space will be described in the following paragraphs. As shown in Figure 2-1, the model features five conical loci: the narrow conical Yield Surface (YS) centred along its axis, the Critical state Surface (CS), Bounding Surface (BS), and Dilatancy Surface (DS) centred along the p-axis and the newly defined MS. The MS, representing the stress ratios previously experienced by the soil, undergoes kinematic hardening, similar to the YS. It also can expand and shrink to simulate the formation and damage of soil’s fabric.

The projection of the critical state line (CSL) in the void ratio, e,– mean effective stress, p, is specifically expressed as follows:

$$e_{cs} = e_0 - \lambda \left(\frac{p}{p_{atm}}\right)^{\xi} \qquad \textit{Eq. 2-1}$$

where p_{atm} is the atmospheric pressure, λ and ξ are model parameters affecting the shape of the CSL and e_0 represents the void ratio at $p = 0\ kPa$ (Figure 2-1).

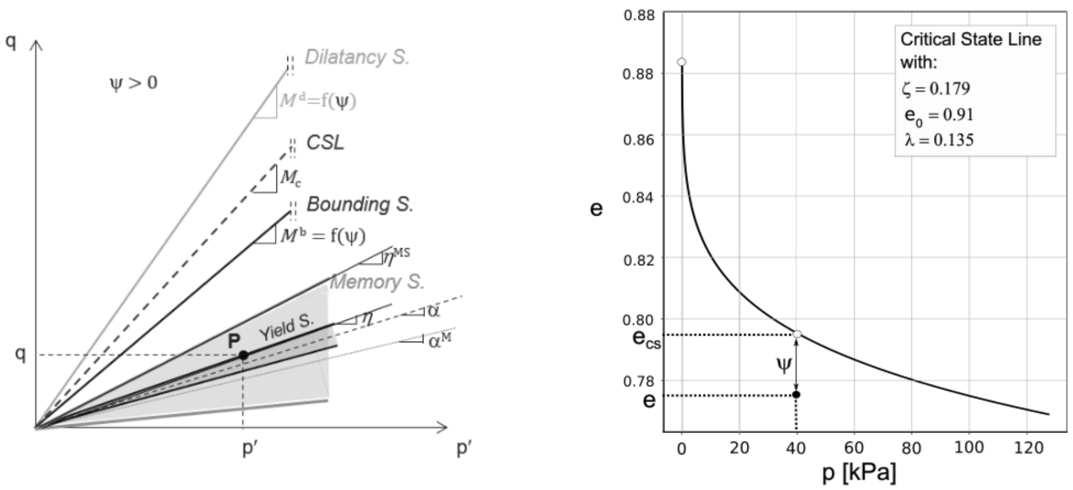

Figure 2-1 Schematic illustration of the model surfaces in triaxial compression (left). CSL in the $e - p$ plane (right)

In the deviatoric stress, q, – mean effective stress, p, plane, the CSL is defined by the equation:

$$q = M_c p \qquad \text{Eq. 2-2}$$

where:

$$M_c = \frac{6 \cdot \sin(\varphi_c)}{3 - \sin(\varphi_c)} \qquad \text{Eq. 2-3}$$

with M_c being a model parameter representing the stress ratio at critical state in triaxial compression and φ_c the corresponding friction angle.

The model uses the concept of state parameter, ψ, (Been and Jefferies, 1985):

$$\psi = e - e_{cs} \qquad \text{Eq. 2-4}$$

where e is the current void ratio and e_{cs} is the void ratio on the CSL computed with the current mean pressure p.

Sizes of both bounding surface (BS) and dilatancy surface (DS), which respectively represent the potential peak and phase transformation stress ratios, evolve with ψ through the bounding and dilatancy stress ratios, M^b and M^d (Figure 2-1). Specifically, the evolution of M^b and M^d is defined as:

$$M^b = M_c \cdot exp(-n^b \psi) \qquad \text{Eq. 2-5}$$

$$M^d = M_c \cdot exp(n^d \psi) \qquad \text{Eq. 2-6}$$

with n^b and n^d being model parameters. The peak shear strength and phase transformation stress ratio are mobilised when $\eta \geq M^b$ or $\eta = M^d$. In the basic SANISAND framework, the hardening modulus, K_p, and the dilatancy, D, are proportional to the distance between the current stress ratio η and its corresponding image on the BS and DS, respectively. In Figure 2-1 (in triaxial conditions), the images simply coincide with M^b and M^d .

In SANISAND-MS, the YS is enclosed inside the MS, as shown in Figure 2-1. The current distance between the stress ratio η and its image on the memory, denoted as η^M in Figure 2-1, is a new key contribution to the hardening modulus and dilatancy in the bounding surface model.

If the YS is tangent to the MS, the stiffness and plastic strains coincide with the ones predicted by SANISAND04. Such a condition will be named as “virgin loading” condition and is a characteristic of monotonic loading.

In cyclic conditions, the distance between η and η^M usually keeps changing from the first unloading. The hardening modulus K_p is increased with that distance, which allows for simulating the increase in soil stiffness experimentally observed under repeated loadings (Figure 1-2) and explained by the build-up of the soil fabric. The memory surface affects both K_p and D, additionally, its effect is triggered right after the first unloading, regardless for the kind of volumetric behaviour (unless a virgin loading condition is restored). This is different from what happens for the dilatancy fabric tensor of SANISAND04 where the effect on D is only activated after the first triggering of a dilative response.

The formulation presented in the next paragraphs differs slightly from that proposed by Liu et al. (2019), firstly by using the concept of yield back stress ratio, $\boldsymbol{\alpha}$. Additionally, it introduces some modifications aimed at improving the stability of the constitutive model when applied to the simulation of boundary value problems.

2.1.1. Yield, critical state, bounding and dilatancy surfaces

The conical model surfaces have been already introduced in the q-p plane in the previous paragraph. Since the plastic behaviour is solely activated when the stress ratio changes, it is convenient to represent the model surfaces in the π-plane of the stress ratio space (Figure 2-2).

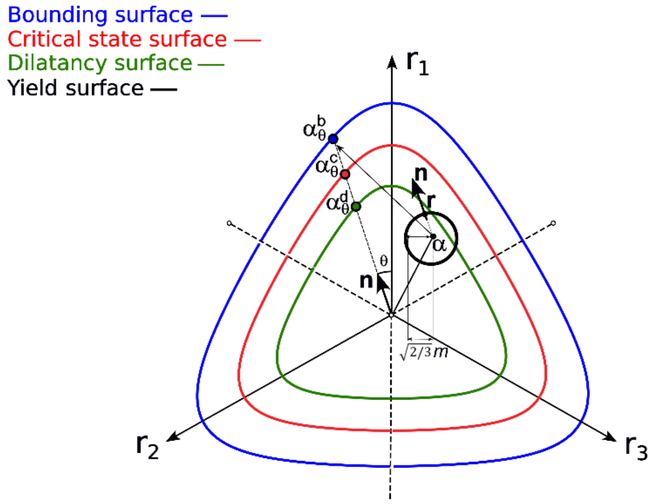

Figure 2-2 SANISAND-MS loci inherited from DM04 in the deviatoric stress ratio plane.

In this space, the yield surface is defined as:

$$f = [(\boldsymbol{r} - \boldsymbol{\alpha}):(\boldsymbol{r} - \boldsymbol{\alpha})]^{1/2} - \sqrt{2/3}\ m = 0 \qquad \textit{Eq. 2-7}$$

where the tensor $\boldsymbol{\alpha}$ is the hardening variable (back stress ratio) defining the position of the axis of the yield surface, $\boldsymbol{r}$ is the current stress ratio, and m is a model parameter determining the size of the yield surface (Figure 2-2).

The tensor $\boldsymbol{n}$ represents the deviatoric unit normal to the yield surface:

$$\boldsymbol{n} = \frac{\partial f}{\partial \boldsymbol{s}} = \left[\frac{\boldsymbol{r} - \boldsymbol{\alpha}}{\sqrt{2/3}\ m}\right]. \qquad \textit{Eq. 2-8}$$

In the current implementation, the shape of the critical, bounding, and dilatancy surfaces, in the π plane, are given by the van Eekelen function (van Eekelen, 1980):

$$g(\theta) = \alpha(1 + \beta\ cos3\theta)^{n} \qquad \textit{Eq. 2-9}$$

Where:

$$\alpha = \left(1 + c^{1/n}\right)^{n}$$

$$\beta = \frac{\left(1 - c^{1/n}\right).}{\left(1 + c^{1/n}\right)}$$

$c = M_e/M_c$ is a model parameter and $n = -1/4$. When compared with the Argyris function (used in Liu et al. 2019 and SANISAND04), the Van Eekelen surface has a broader range of c values that guarantees convexity and therefore allows for more flexibility in the calibration.

The Lode angle used in Eq. 2-9 varies between $\theta = 0°$ in triaxial compression and $\theta = 60°$ in triaxial extension and it is defined in terms of the deviatoric unit tensor $\boldsymbol{n}$, as shown in Figure 2-2. By substituting $\boldsymbol{n}$ in Eq. 2-8 the Lode angle can be rewritten as:

$$cos(3\theta) = \sqrt{6}\, tr(\boldsymbol{n^3})$$ Eq. 2-10

The use of $\boldsymbol{n}$ to compute the Lode angle implies that triaxial conditions are reached when $\boldsymbol{n}$ is aligned with one of the principal axes and not necessarily when $\boldsymbol{r}$ lies on the principal axes in Figure 2-2.

The concepts of image stress ratio tensors (on the CS, DS, and BS) are defined in terms of back stress ratio, as:

$$\boldsymbol{\alpha}_\theta^c = \sqrt{2/3}\,(M_c - m)\, g(\theta)\boldsymbol{n}$$ Eq. 2-11

Similarly

$$\boldsymbol{\alpha}_\theta^d = \sqrt{2/3}\,(M^d - m)\, g(\theta)\boldsymbol{n}$$ Eq. 2-12

$$\boldsymbol{\alpha}_\theta^b = \sqrt{2/3}\,(M^b - m)\, g(\theta)\boldsymbol{n}$$ Eq. 2-13

2.1.2. Memory surface

Analytically, the memory surface is a conical surface defined as:

$$f^M = \sqrt{(\boldsymbol{r} - \boldsymbol{\alpha^M}):(\boldsymbol{r} - p\boldsymbol{\alpha^M})} - \sqrt{2/3}\ m^M = 0$$ Eq. 2-14

where $\boldsymbol{\alpha^M}$ **(**the memory back stress ratio tensor) and m^M represent two variables indicating the position and the size of the MS.

The image stress ratio tensor on the memory surface, defined in terms of back stress ratio, is:

$$\boldsymbol{r}_\alpha^{\mathrm{M}} = \boldsymbol{\alpha^M} + \sqrt{2/3}[m^M\ -\ m]\boldsymbol{n}\,,$$ Eq. 2-15

Figure 2-3 shows the memory surface on the π plane and relevant image conditions used in the kinematic and isotropic hardening rules of the MS, and in the flow rule and YS hardening rule.

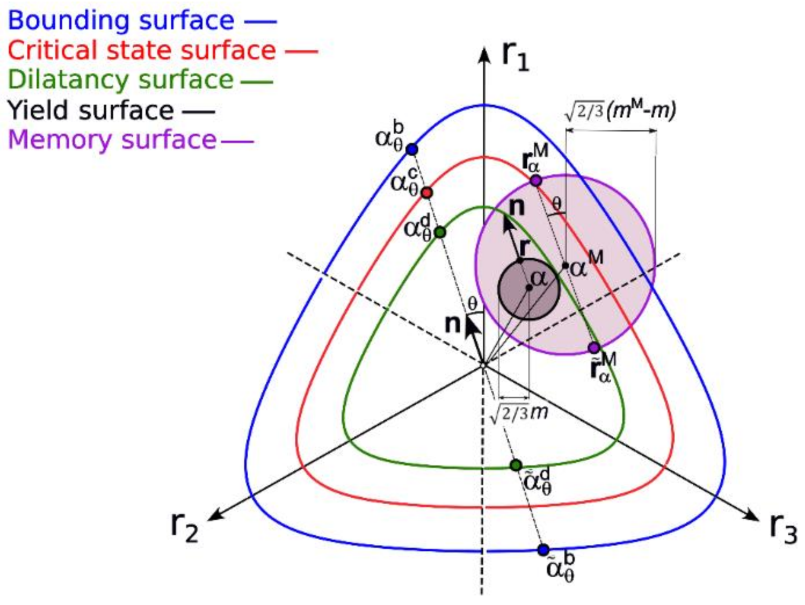

Figure 2-3 Memory surface and image states used in the: MS (kinematic and isotropic) hardening rules, YS (kinematic) hardening rule and in the flow rule.

2.2 Hardening rule

The yield surface evolves according to a rotational hardening mechanism governed by an incremental variation of the back-stress ratio tensor in line with the hardening rule defined in Dafalias and Manzari (2004).

$$\dot{\boldsymbol{\alpha}} = \langle L \rangle h\left(\boldsymbol{\alpha}_\theta^b - \boldsymbol{\alpha}\right), \qquad \textit{Eq. 2-16}$$

This equation states that the rotation of the back stress ratio depends on the distance between the current back stress ratio and the image of the stress on the bounding surface $\boldsymbol{\alpha}_\theta^b$ (see equation), as originally established by the bounding surface plasticity framework.

Having defined the hardening rule, and according to the general principles of the elastoplasticity, it is possible to describe the plastic modulus, K_p, as:

$$K_p = (2/3)ph\left(\boldsymbol{\alpha}_{\boldsymbol{\theta}}^{\boldsymbol{b}} - \boldsymbol{\alpha}\right):\boldsymbol{n} \qquad \textit{Eq. 2-17}$$

where the hardening coefficient, h, is formulated as:

$$h = \frac{b_0}{(\boldsymbol{\alpha} - \boldsymbol{\alpha}_{ini}):\boldsymbol{n} + C_\varepsilon} \, exp\left(\mu_0 \sqrt{\left(\frac{p}{p_{atm}}\right)} \left(\frac{b_\mathrm{M}}{b_{ref}}\right)^2\right) \qquad \textit{Eq. 2-18}$$

and:

$$b_M = (\boldsymbol{r}_\alpha^\mathrm{M} - \boldsymbol{\alpha}):\boldsymbol{n} \qquad \textit{Eq. 2-19}$$

$$b_{ref} = \left(\boldsymbol{\alpha}_\theta^\mathrm{b} + \widetilde{\boldsymbol{\alpha}}_\theta^\mathrm{b}\right):\boldsymbol{n} \qquad \textit{Eq. 2-20}$$

$$b_0 = G_0 \, h_0 \, \frac{(1 - c_h e)}{\sqrt{p/p_{atm}}} \qquad \textit{Eq. 2-21}$$

In the previous equations, μ_0 is a specific model parameter for SANISAND-MS that directly influences the ratcheting, as detailed later, while G_0, c_{h0} and h_0 are model parameters already included in the predecessor SANISAND models.

It is important to highlight that the exponential term in Eq. 2-18 introduces the effect of the term b_M representing the distance between the current stress and its image on the memory (see Eq. 2-19 and Figure 2-3) on the hardening coefficient. When $\boldsymbol{\alpha} = \boldsymbol{r}_\alpha^M$, as during virgin loading conditions, it follows that $b_M = 0$ and, consequently there is no effect of the memory on the plastic modulus and that h coincides with the hardening coefficient of the original SANISAND (Dafalias and Manzari, 2004). In the Eq. 2-18, $C_\varepsilon \propto \frac{h_0}{100} = 0.001$ is a small dimensionless quantity used to avoid computational issues for vanishing $(\boldsymbol{\alpha} - \boldsymbol{\alpha}_{ini}):\boldsymbol{n}$. Moreover, it can be observed that an increase in b_M will lead to an increase in the plastic stiffness.

In addition, similar to the former bounding surface plasticity model (Dafalias and Manzari, 2004), throughout loading, the value of the initial back-stress ratio tensor is tracked at every change in loading direction, identified by the condition $(\boldsymbol{\alpha} - \boldsymbol{\alpha}_{ini}):\boldsymbol{n} < \boldsymbol{0}$, and used to compute the hardening modulus (Eq. 2-17). Specifically, the value of $\boldsymbol{\alpha}_{ini}$ is updated to the current value of $\boldsymbol{\alpha}$ when a loading direction reversal is detected.

2.3 Flow rule

The direction of the plastic flow can be decomposed into its deviatoric and volumetric components, as shown in Eq. 2-22, which define, respectively, the directions of the deviatoric and volumetric plastic strain increments.

$$\boldsymbol{R} = \boldsymbol{R}^{\text{¢}} + D\boldsymbol{I} \qquad \textit{Eq. 2-22}$$

The volumetric plastic flow rule is given by:

$$\dot{\varepsilon}_v^{pl} = \langle L \rangle D \qquad \textit{Eq. 2-23}$$

With:

$$D = A_0\left(\boldsymbol{\alpha}_\theta^d - \boldsymbol{\alpha}\right):\boldsymbol{n}\, exp\left(\beta \frac{\langle \tilde{b}_d^M \rangle}{b_{ref}}\right) \qquad \textit{Eq. 2-24}$$

$$\tilde{b}_d^M = \left(\tilde{\boldsymbol{\alpha}}_\theta^d - \boldsymbol{\alpha_{ini}}\right):\boldsymbol{n} \qquad \textit{Eq. 2-25}$$

$$b_{ref} = |\boldsymbol{\alpha}_{ini}| \qquad \textit{Eq. 2-26}$$

where β is a model parameter specific for SANISAND-MS. In the current implementation the definitions in Eq. 2-25 and Eq. 2-26 differ from Liu et al. (2019), where $\tilde{b}_d^M = \left(\tilde{\boldsymbol{\alpha}}_\theta^d - \tilde{\boldsymbol{r}}_\alpha^{\mathrm{M}}\right):\boldsymbol{n}$, and b_{ref} derives from Eq. 2-20. In Liu et al. (2019), the exponential term in Eq. 2-24 represents the direct effect of the distance between the images of the stress respectively on the MS and on DS. Moreover, note that for applications under drained conditions (as suggested for this model) β does not affect the cyclic response, as detailed in Section 3.1.5. Finally, note that dilation occurs every time $(\boldsymbol{\alpha}^d - \boldsymbol{\alpha}):\boldsymbol{n} < \boldsymbol{0}$.

Regarding the deviatoric plastic flow rule, it is given by:

$$\dot{\boldsymbol{e}}^{pl} = \langle L \rangle \boldsymbol{R}^{\text{¢}} \qquad \textit{Eq. 2-27}$$

where $\boldsymbol{R}^{\text{¢}}$ is formulated as being normal to the critical state surface at the image stress, as given by:

$$\boldsymbol{R}^{\text{¢}} = B\boldsymbol{n} - C\left[\boldsymbol{n}^{\boldsymbol{2}} - \frac{1}{3}\boldsymbol{I}\right] \qquad \textit{Eq. 2-28}$$

with:

$$\mathrm{B} = 1 + \frac{3}{2}\frac{(1-c)}{c} g(\theta) cos(3\theta) \qquad \textit{Eq. 2-29}$$

$$\mathrm{C} = 3\sqrt{3/2}\frac{(1-c)}{c} g(\theta) \qquad \textit{Eq. 2-30}$$

2.4 Memory surface evolution

The memory surface is subjected to isotropic and kinematic hardening. In this paragraph, the equation defining the evolution of the hardening variable m^M and $\boldsymbol{\alpha}^M$, related with the MS, are described. Three assumptions concern the evolution of the memory surface

1. It can expand (with soil contraction) and shrink (with soil dilation) to reproduce the formation and loss of a soil structure, respectively.
2. It must enclose the yield, meaning the YS can never even partially intersect the MS.
3. Its size can never be smaller than the YS size

The isotropic hardening of the memory surface is defined as:

$$dm^M = dm_+^M + dm_-^M \qquad \textit{Eq. 2-31}$$

Where dm_+^M and dm_-^M represent the contributions to the expansion and shrinkage. To ensure that the condition 2 is satisfied during a plastic loading, the translation of the MS must be related to the expansion of the memory (and the kinematic hardening of the YS). The MS is therefore firstly defined, and then used to derive $d\boldsymbol{\alpha}^{\boldsymbol{M}}$.

Memory surface expansion

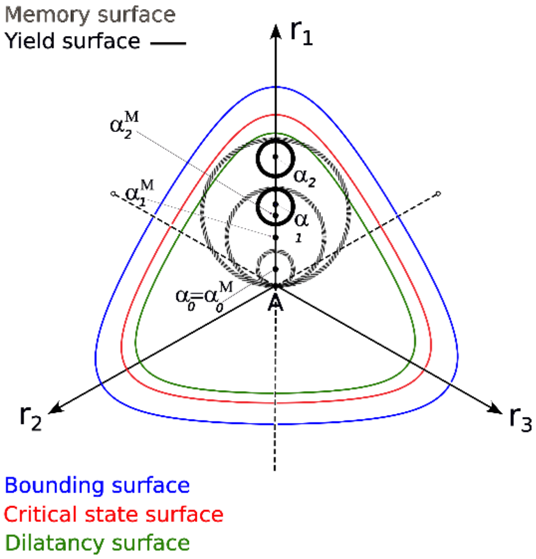

Figure 2-4 Evolution of the memory surface: memory surface translation and expansion in virgin loading conditions

The expression of dm_+^M (expansion of the MS) is derived by assuming the hypothesis of "virgin loading conditions" (YS tangent to MS starting from YS coincident to the MS) in a regime of contractive volumetric response (YS inside the DS) as in Figure 2-4. In this scenario, to ensure that the YS can translate remaining inside the MS, Liu et al. (2019) assume that the MS expands around the point diametrically opposed to the current stress (pivot point A in Figure 2-4). By enforcing the consistency condition for the memory surface in point A (see Appendix), it can be written:

$$dm_+^M = \sqrt{\frac{3}{2}}\, d\boldsymbol{\alpha}^M : \boldsymbol{n} \qquad \text{Eq. 2-32}$$

Based on the previous equation, (as also shown for a triaxial compression Figure 2-4) it is evident that the expansion and the translation of the MS are related.

Memory surface shrinkage

The shrinkage of the memory is formulated as:

$$dm_-^M = -\left(\frac{m^M}{\zeta}\right) f_{shr} \langle -d\varepsilon_{vol}^p \rangle \qquad \text{Eq. 2-33}$$

Where ζ is the third specific model parameter for SANISAND-MS (i.e. not included in the predecessor SANISAND version). ζ directly influences the velocity of de-structuration and, indirectly, the ratcheting. As anticipated, Eq. 2-33 shows that the contraction of the memory occurs only in presence of a dilative behaviour, which is relevant for the calibration of ζ. An example of MS contraction is shown in Figure 2-5 where the MS lies outside the DS allowing for $\langle -d\varepsilon_{vol}^p \rangle$ non-zero. The MS is represented before and after the contraction, which by hypothesis occurs every time around the pivot point $\boldsymbol{r}^{\boldsymbol{M}}$. The coefficient f_{shr} is a term proposed by Liu et al. (2019), to guarantee that during the shrinkage the MS never reduces more than the YS. It is specifically defined as:

$$f_{shr} = 1 - \frac{(x_1 + x_2)}{x_3} \qquad \text{Eq. 2-34}$$

Where:

$$x_1 = \boldsymbol{n}^{\boldsymbol{M}} : (\boldsymbol{r}^{\boldsymbol{M}} - \boldsymbol{r}), \quad x_2 = \boldsymbol{n}^{\boldsymbol{M}} : (\boldsymbol{r} - \tilde{\boldsymbol{r}}), \quad x_3 = \mathbf{n}^M : (\boldsymbol{r}^{\boldsymbol{M}} - \tilde{\boldsymbol{r}}^{\boldsymbol{M}}) \qquad \text{Eq. 2-35}$$

$$\mathbf{n}^M = \frac{(\boldsymbol{r} - \boldsymbol{r}^M)}{|\boldsymbol{r} - \boldsymbol{r}^M|}$$ *Eq. 2-36*

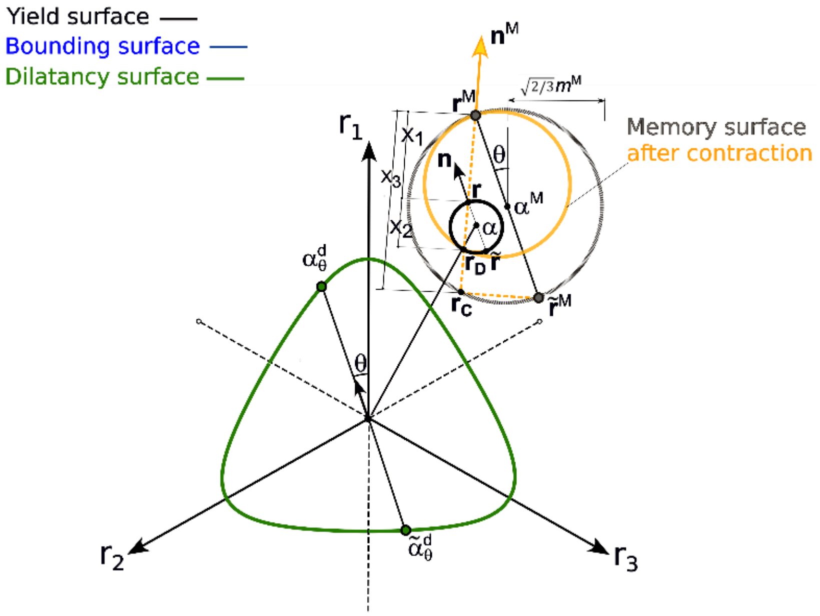

Figure 2-5 Memory surface contraction

The meaning of the terms in the definition of f_{shr} is illustrated in Figure 2-5. It can be observed that the term $\mathbf{n}^M$ represents the direction of the vector connecting the current stress and its image on the MS, which is used by Liu et al. (2019) in Eq. 2-35 to evaluate the difference in sizes of the MS and YS. From Figure 2-5, it is seen that the MS and YS are tangent when $\mathrm{x}_1 + \mathrm{x}_2 = \mathrm{x}_3$. The latter condition leads to $f_{shr} = 0$, which prevents a further contraction of the MS.

Memory surface translation

The kinematic hardening law of the MS is based on the Mroz et al. (1979) rule and considers the memory translation towards the image of the stress on the bounding surface, as given by:

$$d\boldsymbol{\alpha}^{\boldsymbol{M}} = \frac{2}{3}\langle L^M\rangle\, h^M\left(\boldsymbol{\alpha}_\theta^b - \boldsymbol{r}_\alpha^M\right)$$ *Eq. 2-37*

In the equation, h^M and L^M are the hardening coefficient and the plastic multiplier of the MS, respectively. In the current formulation (Liu et al, 2019), the expression of h^M is derived under the hypothesis that the hardening process occurs during virgin loading conditions where the YS and MS are tangent, and that $L^M = L$. In Appendix B, detailed mathematical derivations show how, by enforcing the consistency condition in the tangent point and using both equations of MS isotropic hardening and YS kinematic hardening, the movement of the MS is linked to the YS hardening, and the coefficient can be written as:

$$h^M = \frac{1}{2}\left[\frac{b_0}{(\boldsymbol{r}_{\boldsymbol{\alpha}}^M - \boldsymbol{\alpha}_{\boldsymbol{ini}}) : \boldsymbol{n} + C_\varepsilon} + \sqrt{\frac{3}{2}}\,\frac{m^M f_{shr}\langle -D\rangle}{\zeta(\boldsymbol{\alpha}_{\boldsymbol{\theta}}^b - \boldsymbol{r}_{\boldsymbol{\alpha}}^M) : \boldsymbol{n}}\right],$$ *Eq. 2-38*

with

$$b_0 = G_0\, h_0\, \frac{(1 - c_{h0} e)}{\sqrt{p/p_{atm}}},$$ *Eq. 2-39*

Where G_0 and c_{h0} are material parameters. The first term in Eq. 2-37 shows that, for contractive behaviour, the translation of the MS centre is half YS translation (Figure 2-3). It is worth noticing that the hypothesis of $L^M = L$ is extended to the whole stress history during the plastic flow even for general loading conditions.

2.5 Elasticity

An isotropic hypoelastic model is considered for the elastic component of the model SANISANDMS. The elastic shear modulus depends on both the mean effective stress and void ratio, as given by:

$$G = G_0 p_{atm} \left[\frac{(2.97 - e)^2}{(1 + e)} \right] \left(\frac{p}{p_{atm}} \right)^{0.5} \quad \textit{Eq. 2-40}$$

where G_0 is the dimensionless small strain shear stiffness parameter. A constant Poisson's ratio ν is assumed as a model parameter. Therefore, the elastic bulk modulus can be determined from the shear modulus and Poisson's ratio as:

$$K = \frac{2}{3} \left(\frac{1 + \nu}{1 - 2\nu} \right) G \quad \textit{Eq. 2-41}$$

3.

Model parameters and user defined state variables

3.1 Model Parameters

SANISAND-MS is implemented as a User Defined Soil Model (UDSM) in PLAXIS 3D. In this section, a detailed description of the input parameters is presented. Figure 3-1 shows the list of input parameters in the Material data set window.

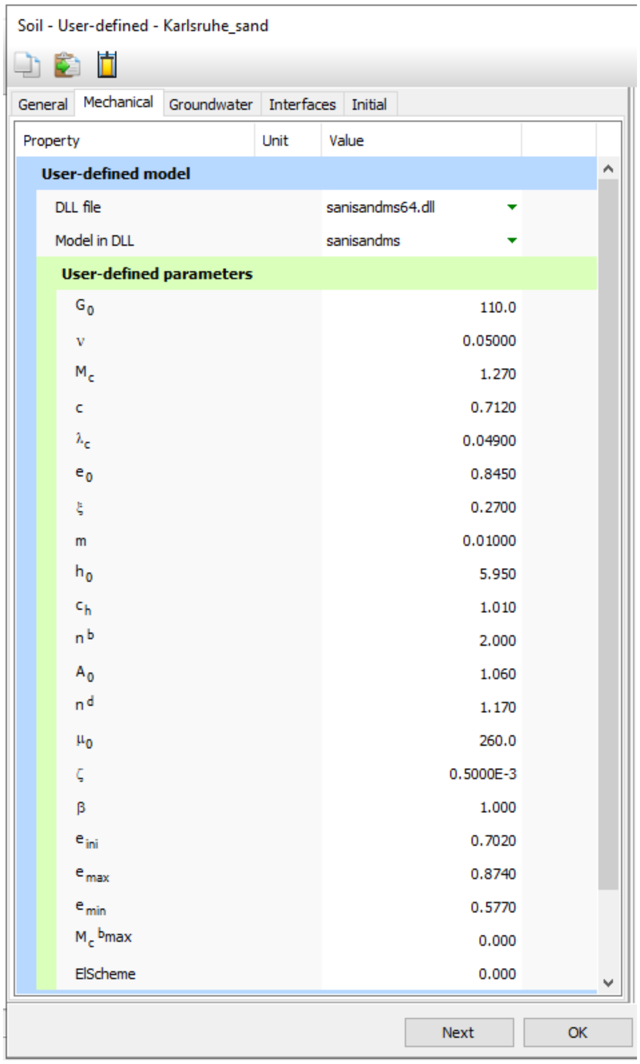

Figure 3-1 Parameters of PLAXIS UDSM SANISANS-MS model in the Material data set window

The PLAXIS SANISAND-MS has 21 input parameters. The first 16 parameters are originally introduced by (Liu et al., 2019), including 13 constitutive parameters of the SANISAND04 and 3 other parameters related to the MS and ratcheting effect. The last 4 parameters (e_{min}, e_{max}, $M_c^b{}_{max}$ and Elscheme) are newly introduced essentially to improve the numerical accuracy and instability of the model in FEA. The calibration and meaning of all the parameters will be described in the following paragraphs.

According to (Liu et al., (2019), the calibration of the 16 constitutive parameters can be performed in two steps: first, the 13 parameters inherited from the SANISAND04 model, and then the parameters specific of SANISAND-MS. Set of parameters presented for the same sand in other studies for SANISAND04 can be adopted for the first 13 parameters, as a first trial.

3.1.1. Critical state locus: $e_{0,}\ \lambda,\ \xi,\ M_c,\ c$

The parameters $e_{0,}$ λ and ξ define the shape of the CSL in the compressibility plane. Preferably, their values can be determined from results of drained triaxial tests performed on loose samples (Jefferies and Been, 2016). In Figure 3-2 (left), the continuous lines represent the CSL as calibrated for Karlsruhe and Toyoura sands (Liu et al., 2019). The dashed lines show the effect of parameters λ and ξ on the trend.

The stress ratios at critical state in triaxial compression, M_c , and in triaxial extension, M_e , are usually simpler to be estimated from stress paths and/or stress ratio–strain responses. A weak dependence of the friction angle at critical state on the Lode angle is experimentally observed in sands. In Eq. 2-9, the dependence of φ_c from θ is controlled by the parameter c. Calibrated values of c are often close to 0.7. Figure 3-2 (right) shows the trend for three values of c.

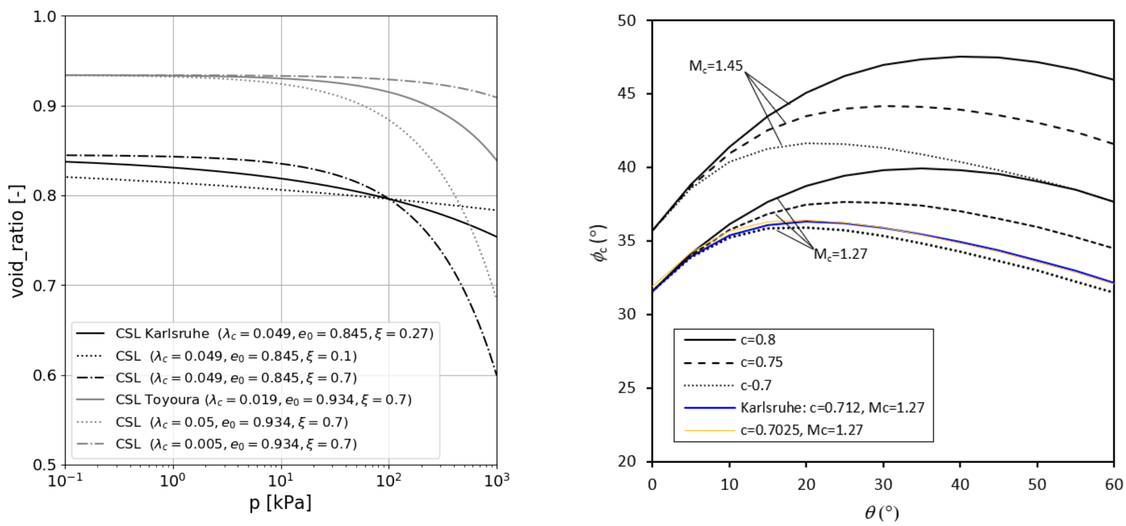

Figure 3-2 (left) Effect of variations in ξ and λ_c on the trend of the CSL calibrated for Karlsruhe and Toyoura sand, respectively. The continuous lines are obtained with the calibrated parameters (Liu et al., 2019). (right) Variability of the friction angle at critical state with the Lode angle along the function of Eq. 2.9, where $n = -1/4$: effect of different c values on the trend

3.1.2. Bounding and dilatancy surfaces: $n^b,\ n^d$

The parameters n^b and n^d control the dependency of bounding and dilatancy stress ratios, (Eq. 2-5 and Eq. 2-6) on the state parameter ψ. These parameters can be calculated from the interpretation of laboratory test results of monotonic triaxial tests, considering that the peak and phase transformation are mobilized respectively when $\eta = M^b$ and $\eta = M^d$. More specifically, by knowing the state parameters at the peak and phase transformation conditions, $\psi^b\ and\ \psi^d$ respectively; and the corresponding stress ratios, the model parameters n^b and n^d can be evaluated from the Eq. 2-5 and Eq. 2-6. Figure 3-3 shows an example of calibration for Toyoura sand presented in Taiebat and Dafalias, (2008).

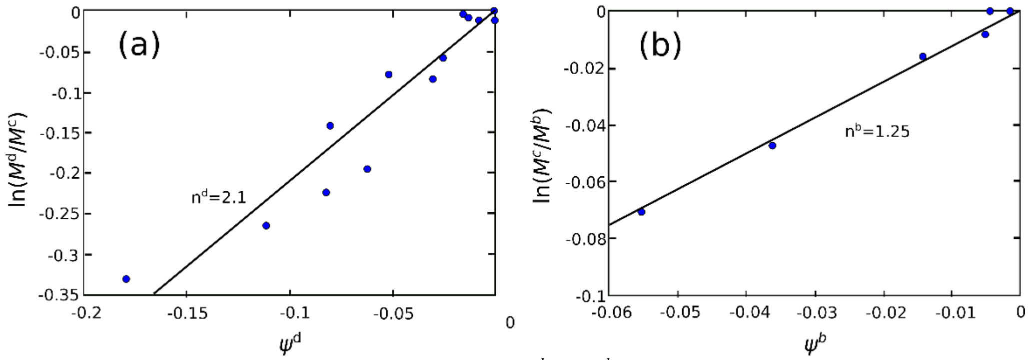

Figure 3-3 Example of calibration of model parameters n^d and n^b for Toyoura sand (adapted from Taiebat and Dafalias, 2008). Data after Verdugo and Ishihara (1996)

3.1.3. Hardening and dilatancy coefficients: h_0, c_h, A_0

Parameters h_0 and c_h in Eq. 2-18, influence the magnitude of the plastic modulus K_p and the effect of the soil density on K_p. They can be determined through an iterative procedure to best fit the deviatoric stress–axial strain, $\varepsilon_a - q$, trend observed in monotonic triaxial tests performed on samples with different initial void ratios and consolidation effective stresses. The parameter A_0 affecting the dilatancy coefficient, D (Eq. 2-24), could be directly estimated from the interpretation of monotonic drained triaxial tests. In Eq. 2-24, the contribution to D due to the MS formulation can be disregarded, and the equation can be rewritten as

$$D = \sqrt{\frac{2}{3}} A_0 (M^d - \eta) \qquad \text{Eq. 3-1}$$

Having considered that $\alpha^d = M^d - m$, and that $\alpha = \eta - m$. As suggested by Manzari and Dafalias, (2004), $d = \sqrt{2/3} A_0$ can be derived from the laboratory tests. As suggested by Been and Jefferies, 2004, assuming that the elastic strain can be disregarded, the dilatancy can be approximated with a central-difference approximation as:

$$D_j = \frac{\varepsilon_{v,j+1} - \varepsilon_{v,j-1}}{\varepsilon_{q,j+1} - \varepsilon_{q,j-1}} \qquad \text{Eq. 3-2}$$

Alternatively, assuming K and G as constants, it can be written:

$$D_j = \frac{(\varepsilon_{v,j+1} - \varepsilon_{v,j-1}) - (p'_{j+1} - p'_{j-1})/K}{(\varepsilon_{q,j+1} - \varepsilon_{q,j-1}) - (q_{j+1} - q_{j-1})/3G} \qquad \text{Eq. 3-3}$$

As shown in Figure 3-4, the plot of the stress ratio $\eta = \frac{q}{p}$ against D allows first to assume a value for M^d (which is the η corresponding to $D = 0$) and then the coefficient d can be simply determined from the slope of the linear part of the trend (in the range of dilative response) considering the definition of D

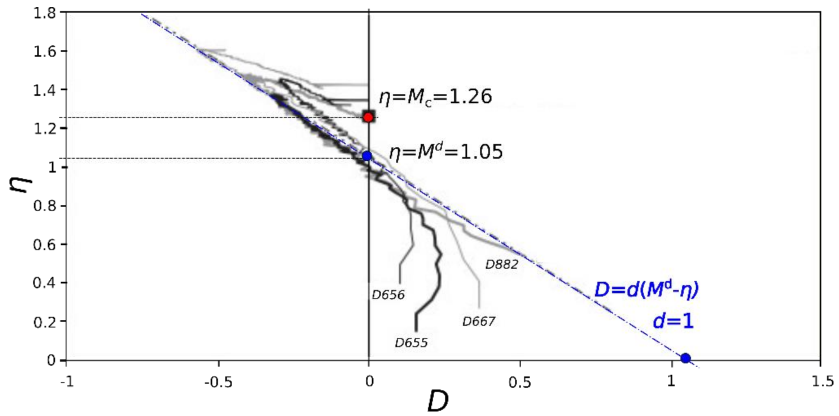

Figure 3-4 Stress ratio-dilatancy relationships from drained triaxial tests on dense samples of Erksak sand: example of calibration of the model parameter A_0 (adapted from Been and Jefferies, 2004)

3.1.4. Elasticity: $\boldsymbol{G_0}$, $\boldsymbol{\upsilon}$, $\boldsymbol{m}$

The dimensionless coefficient G_0 in Eq. 2-40 controls the elastic (small strain) shear modulus, G, and can be calibrated based on laboratory or field tests to fit the shear wave velocity measurement performed with bender elements, resonant column or cross-hole tests, as $G = \rho(V_s)^2$.

G_0 may be calibrated to fit the initial $q-\varepsilon_a$ response in triaxial compression tests (Taiebat and Dafalias, 2008) by considering the effect of the initial shear stiffness on the trend of monotonic triaxial tests. The calibration of G_0 should account for the initial state of the soil, possible discrepancies between the conditions of the soil in situ and reconstituted samples, as well as the early plasticity occurring in the initial part of triaxial tests. For applications in boundary value problems, G_0 should be defined based on the in-situ state of the soil. A calibration approach considering in-situ conditions can be found in Taborda et al., (2020).

An accurate estimation of Poisson's ratio often requires high-resolution local strain measurements, which are not readily available in common practice. However, as highlighted by Loukidis and Salgado, (2009), the Poisson's coefficient does not significantly vary among different types of sands. Typically, the soil skeleton Poisson's ratio for sands falls within the range of 0.1 – 0.3 (Shibuya et al., 1994). In some SANISAND calibrations documented in the literature, a Poisson’s ratio smaller than the measured can be found. For Toyoura sand, for instance, despite values in the range 0.1 – 0.22 are expected, in Dafalias and Manzari (2004) $\upsilon = 0.05$. The discrepancies can be explained with the need to best fit the results of the triaxial tests, which typically do not allow to examine the mechanical response in the purely elastic range.

For the amplitude of the elastic range, Dafalias and Manzari, (2004) suggest m in the order of magnitude of $M_c/100$. This parameter could be increased when a very stiff response is observed in the triaxial tests.

3.1.5. Memory and ratcheting related parameters: $\boldsymbol{\beta}$, $\boldsymbol{\mu_0}$, $\boldsymbol{\zeta}$

The memory and ratcheting related parameters β, μ_0 and ζ have no effect on the mechanical response predicted in drained monotonic loading conditions. Therefore, as aforementioned, they can be calibrated separately from the 13 parameters of the baseline SANISAND04 framework.

β, μ_0 and ζ can be determined from results of drained high cyclic triaxial tests, by fitting of the total accumulated strain ε^{acc} versus the number of loading cycles. The accumulated total strain is defined as:

$$\varepsilon^{acc} = \sqrt{(\varepsilon_a^{acc})^2 + 2(\varepsilon_r^{acc})^2} = \sqrt{\frac{1}{3}(\varepsilon_{vol}^{acc})^2 + \frac{1}{3}\left(\varepsilon_q^{acc}\right)^2} \qquad \text{Eq. 3-4}$$

Where ε_a^{acc}, ε_r^{acc}, ε_{vol}^{acc}, ε_q^{acc} refer to axial, radial, volumetric and deviatoric accumulated strain, respectively. In Eq. 3-4, the accumulated strain is defined by Wichtmann (2005) as the permanent strain accumulated after the first loading cycle. Extensive investigation of the high-cyclic mechanical behaviour of sands is available in the work of Escribano, (2014); Wichtmann, (2005) and calibrations in Liu et al. (2019) and Liu and Pisanò (2019).

Figure 3-5 shows an example of a typical stress path and loading conditions applied for the evaluation of ratcheting accumulated in asymmetric small amplitude stress controlled cyclic triaxial tests. As in Figure 3-5, the drained high cyclic tests are often performed on anisotropically consolidated samples where the target initial conditions of the cyclic triaxial phase, denoted by point B in Figure 3-5, are reached through a *p*-constant shearing phase. Given that the initial void ratio of the tests is available in the initial isotropic condition (A in Figure 3-5), the stress path applied to bring the sample to the initial condition B must be simulated properly to start the cyclic test with a correct initial void ratio. In the following, the characteristics of the tests will be defined through the initial mean effective stress p_{ini} and void ratio e_{ini}, the average stress ratio η_{ave} and the amplitude of the cyclic load $\Delta\eta = \Delta q/p_{ini}$. An explanation of how to perform these tests in PLAXIS SoilTest is provided in Chapter 5.

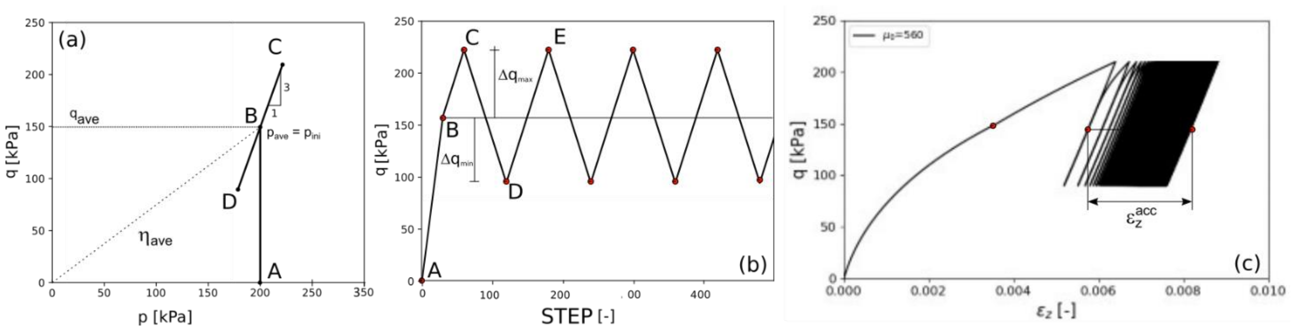

Figure 3-5 Schematic illustration of the stress path applied in typical drained cyclic tests: (a) stress path (b) loading conditions. (c) Accumulated axial strain as reported by Wichtmann (2005).

A strategy for the calibration of these parameters is proposed by Liu et al. (2019). In drained conditions, the calibration process is strongly simplified by the fact that β seems to play a significant role only in undrained simulations. Figure 3-6 shows the trend of accumulated strain, calculated with Eq. 3-4, from simulations performed using the data of Table 3-1 and three significantly different values of β. The results in Figure 3-6 (left) are almost independent of β, conversely, in the undrained tests of Figure 3-6 (rigth), the effect of β on the unloading stress path following a pronounced dilative response can be observed. A choice that has proven convenient in several drained analyses is $\beta = 1$.

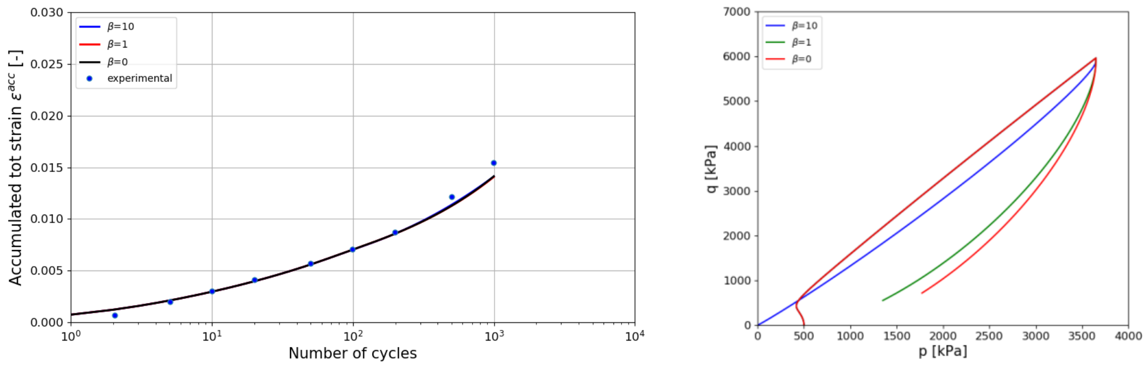

Figure 3-6 Influence of β on the accumulated strain predicted in a cyclic tests in a: (left) drained test with simulation settings: $p_{ini} = 200kPa$, $e_{ini} = 0.68$, $\eta_{ave} = 1.125$, $\Delta\eta = \frac{60}{200} = 0.3$ and (right) in an undrained strain-controlled tests with $p_{ini} = 500kPa$, $e_{ini} = 0.6$, where $\varepsilon_{unldod} = 7\%$

Table 3-1 Karlsruhe Quartz sand (after Liu et al., 2019)

PARAMETER	SYMBOL	VALUE	UNITS
Shear modulus coefficient	G_0	110	-
Poisson's ratio	υ	0.05	-
Stress ratio at critical state in triaxial compression	M_c	1.27	-
Ratio between critical stress ratios in triaxial extension and compression	c	0.712	-
Slope of the CSL in the compressibility plane	λ_c	0.049	-
Void ratio of the CSL at p=0kPa	e_0	0.845	

Critical state line constant	ξ	0.27	-
Size of the yield surface	m	0.01	-
Hardening parameter	h_0	5.95	-
Hardening parameter	c_h	1.01	-
Bounding parameter	n^b	2.0	-
Dilatancy parameter	A_o	1.06	-
Dilatancy surface parameter	n^d	1.17	-
MS surface parameter	μ_0	260	-
MS surface parameter	ζ	0.0005	-
MS surface parameter	β	1	-
Initial void ratio of the layer	e_{ini}	varies	-
Maximum void ratio	e_{max}	0.874	-
Minimum void ratio	e_{min}	0.577	-
Maximum bounding stress ratio in triaxial compression	$M^{b,max}$	0	-
Toggle	Elscheme	0	-

For the calibration, it is also convenient to consider that ζ influences the mechanical response only during dilation (see Eq. 2-33). Therefore, to decouple the effect of ζ and μ_0, and calibrate the parameter μ_0, Liu et al. (2019) suggest (first) simulating a cyclic test with both η_{ave} and $\Delta\eta$ such that the stress ratio does not cross the phase transformation line (i.e. assuming that both ζ and β would have little influence on the results). According to Liu et al. (2019), this should result in a satisfactory prediction of the ratcheting for the samples with contractive volumetric behaviour. Figure 3-7 shows an example of this kind of test. The dashed line in Figure 3-7 represents the critical state line and the green is the phase transformation line (for ψ in the avarage state of the cyclic phase). In the initial isotropic state the void ratio and mean efective stress of the sample are $e_{ini} = 0.702$ and $p_{ini} = 200kPa,$ (Wichtmann, 2005), which, as shown in Figure 3-7 c, correspond to a negative state parameter. The initial condition of the cyclic-phase, is characterized by $p_{ini} = 200kPa$ and a stress ratio $\eta_{ave} = 0.75$. During the cyclic phase, a deviatoric stress oscillation of $q^{ampl} = 60kPa$ is applied, corresponding to $\Delta\eta = 0.3$. As shown in Figure 3-7 a), despite the dense state of the sample, the peak stress ratio, remains smaller than M^d and does not activate a dilative behaviour. Figure 3-7 c) and d) show the actual contractive volumetric behaviour. Figure 3-7 b) and d) allow to visulaze the amplification of the ratcheting produced by an increasing μ_0. Figure 3-8 shows the accumulated strain calculated, with Eq. 3-4, from the output of the three symulations versus the experimental results. A $\mu_0 = 260$ allows to capture the experimental trend.

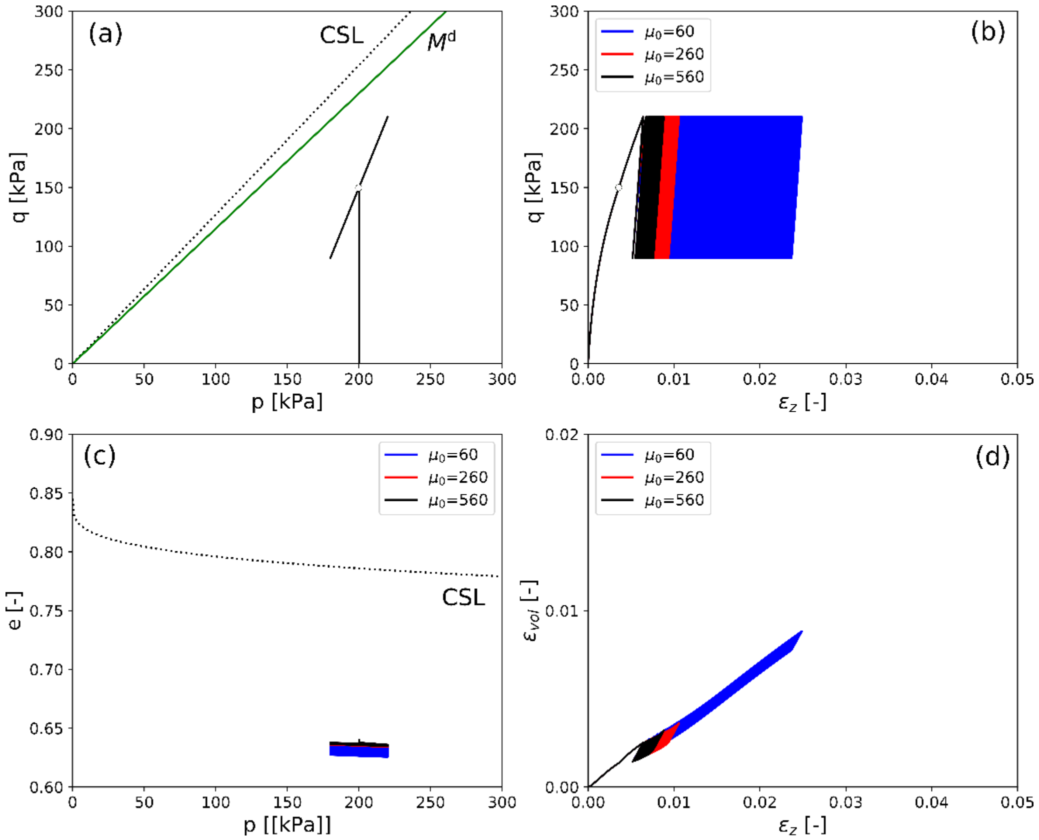

Figure 3-7 Influence of μ_0 on the state path and stress-strain response predicted in cyclic tests. Drained tests with simulation settings: $p_{ini} = 200kPa$, $e_{ini} = 0.702$, $\eta_{ave} = 0.75$, $\Delta\eta = \frac{60}{200} = 0.3$

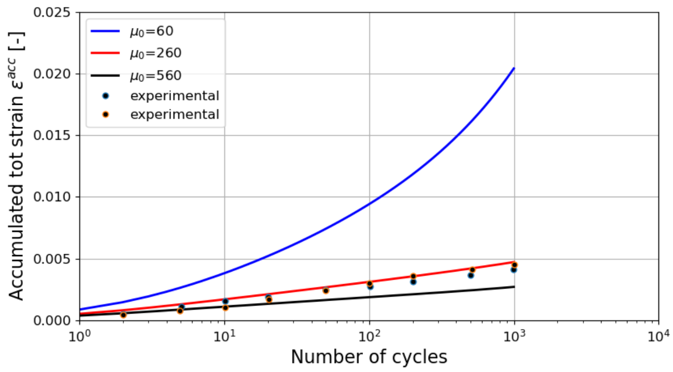

Figure 3-8 Influence of μ_0 on the accumulated strain predicted in predicted in cyclic tests. Drained tests with simulation settings: $p_{ini} = 200kPa$, $e_{ini} = 0.702$, $\eta_{ave} = 0.75$, $\Delta\eta = \frac{60}{200} = 0.3$.

Figure 3-9 shows an example of tests where the dilative mechanical response is activated. Contrarily to Figure 3-7, the stress path crosses the phase transformation line, and consequently, an alternation between dilation and contraction is predicted (Figure 3-9 c) and d)) with an overall accumulation of permanent strains which is considerably influenced by ζ. Figure 3-10 shows the comparison between the accumulated strain resulting from the simulations and the experimental value. An unrealistic overestimation of the permanent strain is observed for ζ excessively small, due to a very quick shrinkage of the memory that restore high deformability.

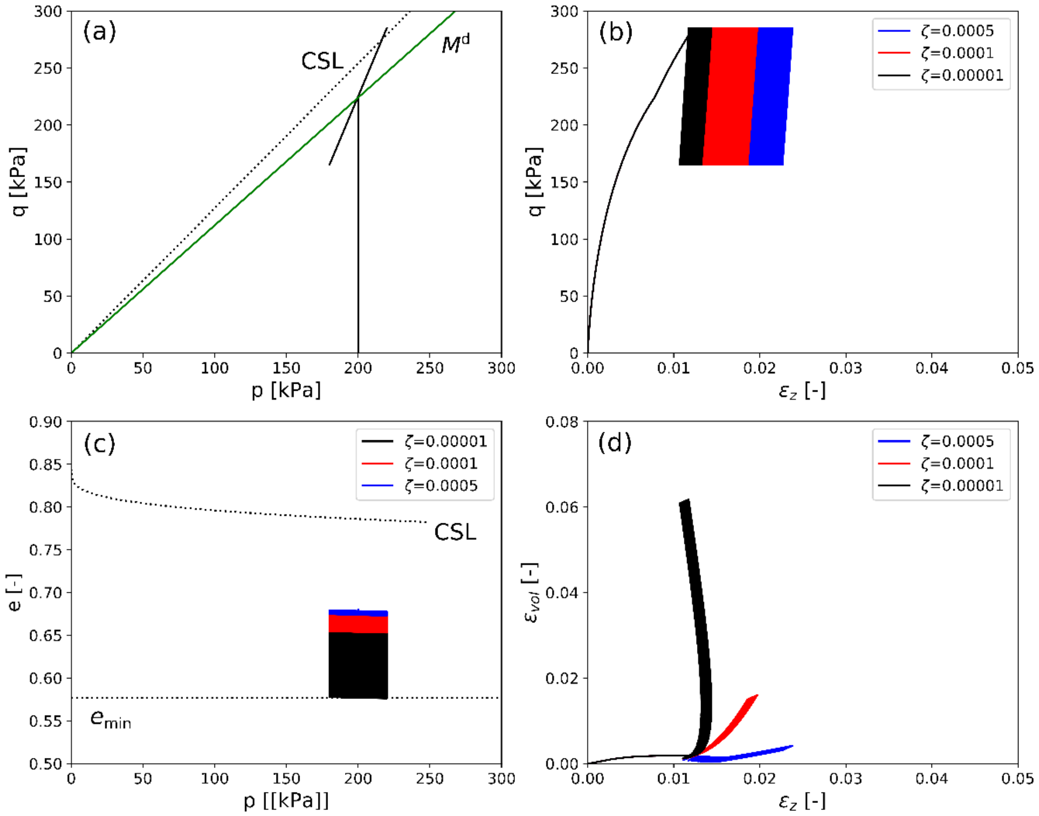

Figure 3-9 Influence of ζ on state path and stress-strain response predicted in cyclic tests. Drained tests with simulation settings: $p_{ini} = 200kPa$, $e_{ini} = 0.68$, $\eta_{ave} = 1.125$, $\Delta\eta = \frac{60}{200} = 0.3$.

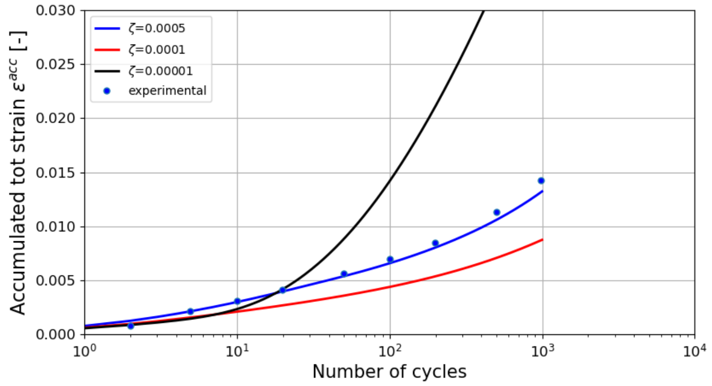

Figure 3-10 Influence of ζ on the accumulated strain predicted in cyclic tests. Drained tests with simulation settings: $p_{ini} = 200kPa$, $e_{ini} = 0.68$, $\eta_{ave} = 1.125$, $\Delta\eta = \frac{60}{200} = 0.3$.

3.1.6. Void ratios: e, e_{min}, e_{max}

The input parameter, e, is the initial void ratio of the soil, which, more than a parameter, represents a state variable. The variability of the void ratio with the depth can be described throughout the definition of multiple material sets. The minimum and maximum void ratios (e_{min} , e_{max}), can be set as the minimum and maximum void ratios for the sand.

3.1.7. Maximum bounding surface: $M_c^{b,max}$

The input parameter $M_c^{b,max}$ is the maximum value allowed for the bounding stress ratio in triaxial compression. In most cases, $M_c^{b,max}$ can be left as 0 to exclude any specific limitation. Setting a value for $M_c^{b,max}$ can help to prevent an excessive expansion of the BS (considering the scaling effect that M^b (Eq. 2-5) has on $\boldsymbol{\alpha}_\theta^b$ in Eq. 2-11) and a potential overestimation of the peak strength. This can be relevant (as shown by Taborda et al., 2020) if very dense initial states must be simulated. As shown for the critical state, the friction angle at failure varies with the Lode angle (Figure 3-2). For particularly dense sands (very small state parameter), the predicted peak friction angle, especially for Lode angles greater than 20°, can reach values greater than 50°. If the peak friction angle predicted (with the calibrated parameters) in drained test (plane strain or extension or $\theta \neq 0°$) for dense sands overestimates the experimental value, $M_c^{b,max}$ can be set to value smaller than $(1.5 - m)/c$, which allows to restrain the peak strength for the others Lode angles. The overestimation of the peak strength can be also emphasized considering that the bounding can be temporarily crossed. Limiting the opening of the BS can (by anticipating the reduction of the stress ratio) prevent that η reaches values corresponding to tensional stresses, which improve the numerical stability.

3.1.8. Elastic scheme toggle

Elscheme is a numerical control toggle, which is set by default to zero. In this case, the stress integration of the elastic behaviour is performed using a single step forward Euler scheme, which should ensure a satisfactory accuracy with low computational resource for most of the normal cases. However, in some cases, elastic nonlinearity accumulation might be more significant, for example when parameter m is very high (in the order of Mc/10) and/or the number of cycles is greater than 1000. In these rarer cases, a higher order integration scheme can be used by setting Elscheme =1 to improve the accuracy of the calculation, but with a potential increase of computation cost.

3.2 User-defined State variables

In PLAXIS Output the user can plot a list of variables related to the model (Figure 3-11). The list includes the hardening variables of the model ($\boldsymbol{\alpha}$, $\boldsymbol{\alpha}^{\boldsymbol{M}}$, m^{M}), other state variables and additional variables that facilitate the interpretation of the results. A description of the variables is provided in Table 3-2.

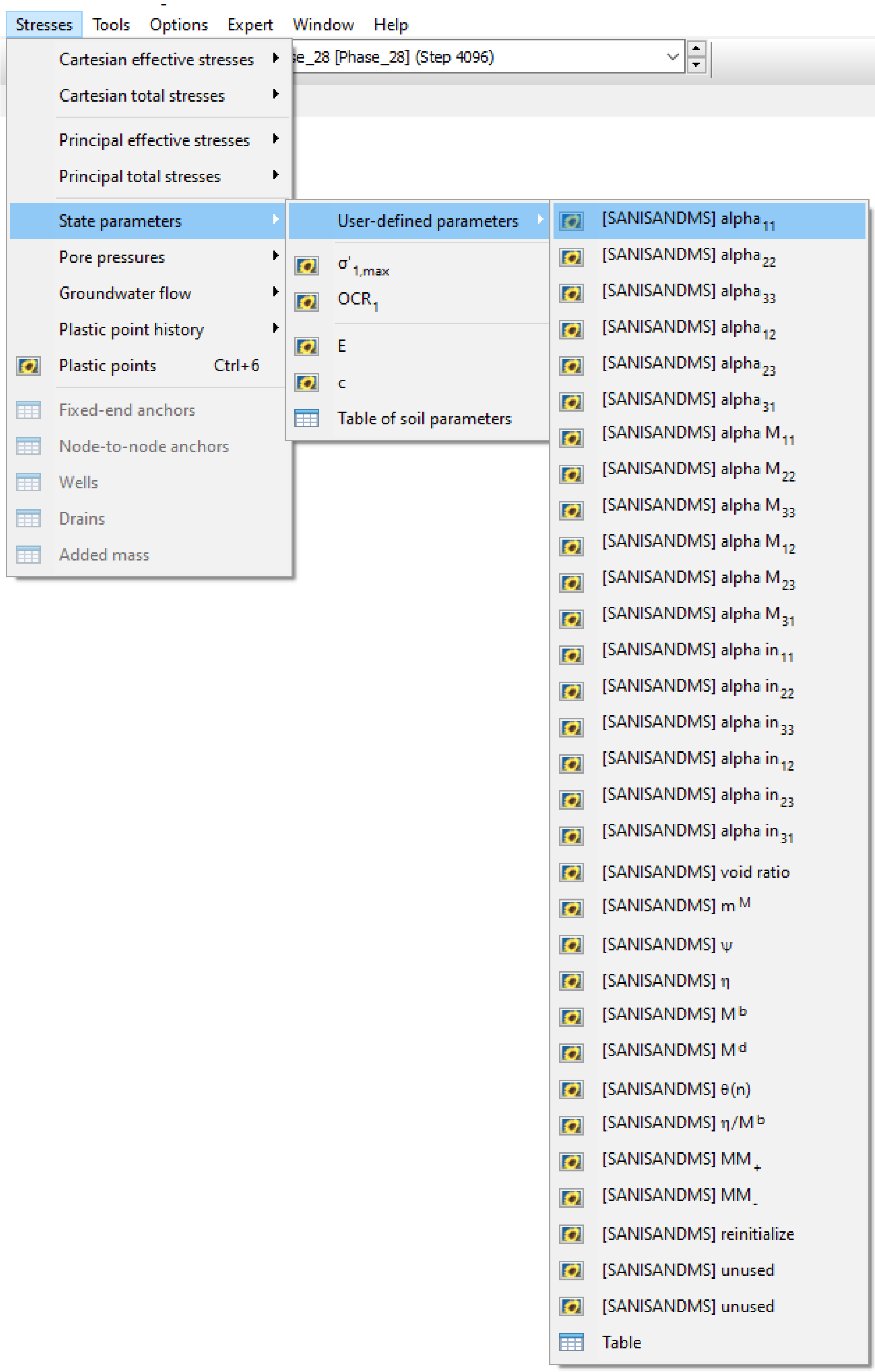

Figure 3-11 State variables of SANISANS-MS.

Table 3-2 User defined State variables

STATE VARIABLE	SYMBOL	DESCRIPTION	UNITS
1→6	$\boldsymbol{\alpha}$	Yield surface back stress ratio	-
7→12	$\boldsymbol{\alpha^M}$	Memory surface back stress ratio	-
13→19	$\boldsymbol{\alpha_{ini}}$	Yield surface back stress ratio at the last detected unloading	-
20	$void\ ratio$	Current void ratio	-
21	m^M	Memory surface radius	-
22	ψ	State parameter (Eq. 2-4)	
23	η	Stress ratio (Eq. A-3)	-
24	M^b	Bounding surface tress ratio for the current value of θ	-
25	M^d	Dilatancy surface tress ratio for the current value of θ	-
26	θ	Lode angle (of **n**) (Eq. 2-9)	°
27	η/M^b	Current stress ratio over the bounding stress ratio	-

4.

Advise on the use of the model

- FE simulation of cyclic laterally loaded monopiles can be performed in PLAXIS 3D with two alternative modelling strategies: dynamic analyses or using a sequence of loading-unloading static which can provide equivalent results. In the first case, loads can be defined through a time history of forces. It is advised to use a frequency small enough to achieve a quasi-static response. In case of analysis aborting with error code 247, inspect the field of the accelerations in output and, in presence of non-irrelevant localized accelerations, reduce the frequency of the input load. Possibly, it is also recommended to split the dynamic simulation in sets of phases to adjust the number of steps required for successfully running the simulation (because dynamic analysis uses a constant time step) and for convenience when inspecting the results. An example is illustrated in Chapter 6. The two kinds of modelling provides results essentially coincident. Recourse to dynamic analyses is convenient for load $\xi_b \leq 25\%$. Extended tests showed that the simulation through sequence of static loading phases allow a considerable advantage in terms of time.

- The initialization of the state parameters is performed only at the first use of the material set parameters (unless reset state is selected). At initialization, the back stress ratio of the YS is set coincident with the current stress ratio tensor. For initialization of the MS, the hypothesis of “virgin loading conditions” is assumed. The opening of the memory surface is assumed coincident with m and its back stress ratio equal to $\boldsymbol{\alpha}$.

- The integration of the elastoplastic strain increment is performed with an explicit integration scheme with automatic sub stepping and error control to enhance accuracy while optimizing computational resources. Elements at the ground surface, especially close to the monopile surface are susceptible to developing large deformations at advanced stages of push-over analyses. Excessive distortion of can cause a premature stoppage of a simulation. The use of a reduced friction angle for the interface elements in a layer having a thickness of 5%L can reduce the localization. The integration can be facilitated by the adoption of a smaller time step or maximum load fraction per step.

- In the SoilTest tabs, a default number of steps per quarter of cycles is predefined. For the simulation of high-cyclic tests (characterized by small amplitude of the loadings and extremely high number of cycles) it is recommended to reduce the number of steps per quarter of cycles. 30 to 50 are usually sufficient to run this kind of simulations without generating too many output data. Possibly, the accuracy of the solution can be improved by setting the elastic param toggle to 1. Stress-controlled tests can lead to failure as the arch length procedure is not active in SoilTest. Therefore, check the monotonic strength before simulating the cyclic tests, and in case of analyses lagging, inspect the input data of the test.

- If the 3D model is generated through the Monopile Designer, an increase in the size of the domain (generated for different typology of constitutive models) is suggested to limiting the effect of the boundaries on the solution. A sensitivity analysis can be performed to evaluate the proper model size for the calculation.

- When running a calculation in PLAXIS 3D, if the analysis stops with error code 247 (Complex error), an extra error number is displayed for iAbort (Figure 4-1). The meaning of the code number for iAbort is described in Table 4-1. If, after following the instructions and inspecting the results and quality of the mesh, the error persists, please contact the Plaxis support team.

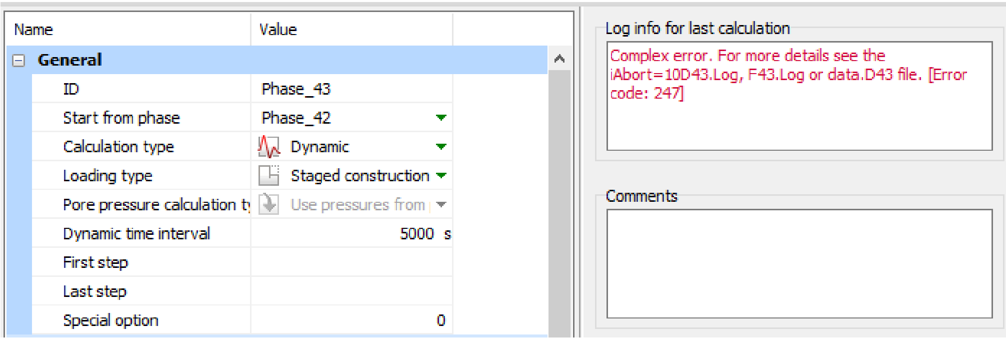

Figure 4-1 Log information in the Phase explorer.

Table 4-1 Description of iAbort UDSM error codes when PLAXIS 3D Error (code 247) is found.

ERROR CODE	DESCRIPTION	ACTION
100	Invalid input parameter	One or more of the 13 SANISAND04 parameters is zero. Inspect the input to find the missing input parameters in the material set
101	Invalid ζ	The MS shrinkage parameter is missing or invalid
102	Inconsistent assignment of current maximum and minimum void ratios	Inspect the input for e_0, e_{min}, e_{max} because $e_{min} \ll e_0 \ll e_{max}$ is not verified
10	In the sub-stepping procedure, the minimum time step has been reached and the effective stress is fully admissible	Reduce the time step of the dynamic analysis or the maximum load fraction per steps (and increase the Max steps) for the plastic analysis
11	In the sub-stepping procedure, the minimum time step has been reached but the stress ratio is associated to tensional stresses	Reduce the time step of the dynamic analysis or the maximum load fraction per steps (and increase the Max steps) for the plastic analysis. If $M_c^{b,max}$ is 0, set it equal to $(1.5 - m)/c$
12, 2, 3, 4, 5, 6, 7, 8 and 9	Numerical issues	These errors should be unlikely to occur. If they are encountered, the operations suggested for ERROR CODE 10 can be adopted. Potentially, a reduction of the ratcheting parameter μ_0 could be tried.

5.

Model response and validation in monotonic and cyclic loading conditions: SoilTests examples

To demonstrate the performance of the model, two sets of monotonic drained triaxial (TX) tests have been simulated through the PLAXIS SoilTest facility by using the calibration proposed in Liu et al. (2019) and reported in Table 3-1. Figure 5-1 shows the results of the first set obtained in three simulations performed with the same initial mean effective stress (200 kPa) and three different initial void ratios: $e_0 = 0.805$, $e_0 = 0.674$, $e_0 = 0.580$. Figure 5-2 shows the comparison between the experimental data and numerical results for the second set of TX compression tests performed with the same initial void ratio $e_0 = 0.69$ and three initial mean effective stresses: $p_0 = 50\ kPa$, $p_0 = 100\ kPa$, $p_0 = 200\ kPa$.

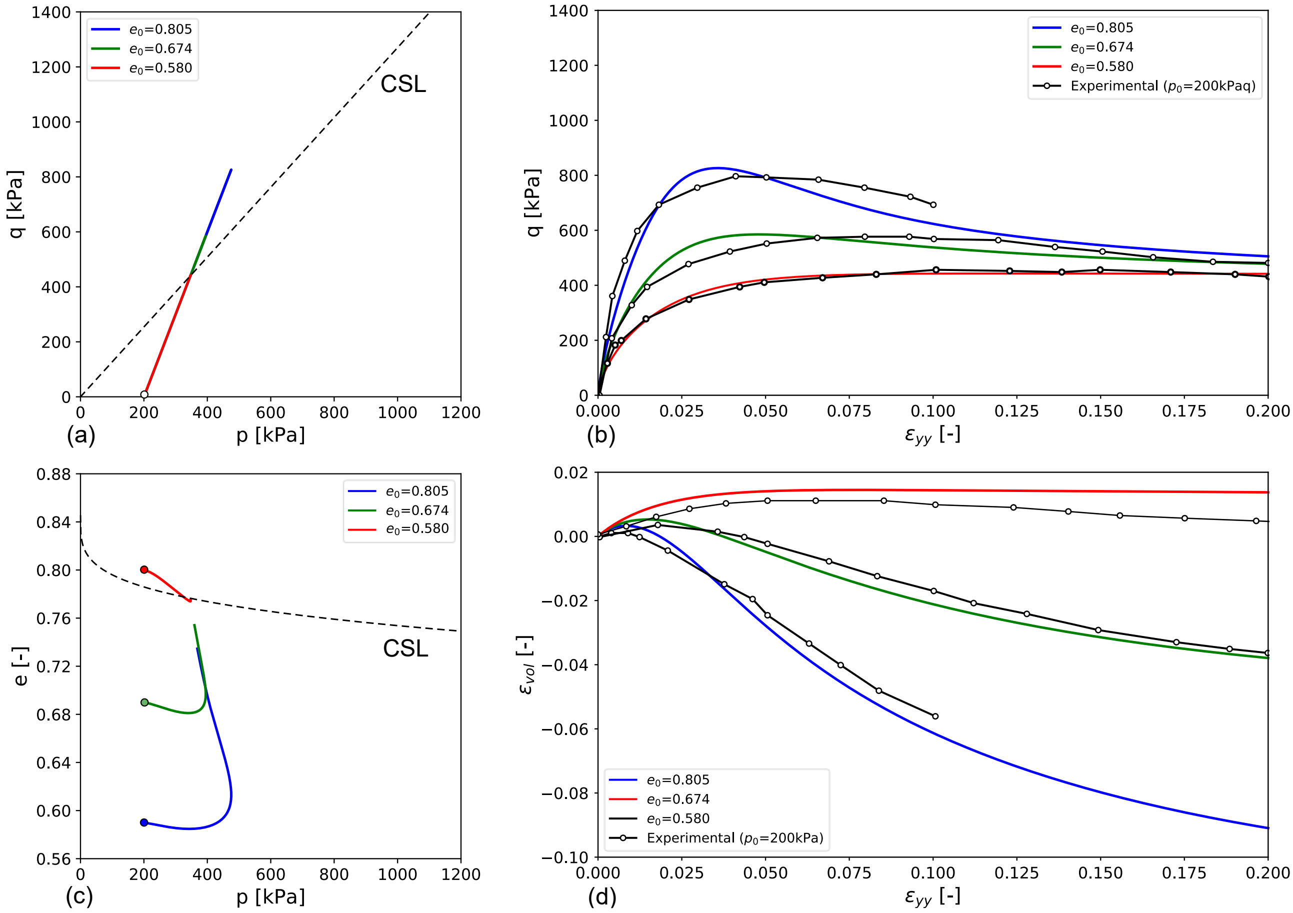

Figure 5-1 Monotonic drained triaxial tests on for varying initial void ratios: comparison between experimental and numerical results.

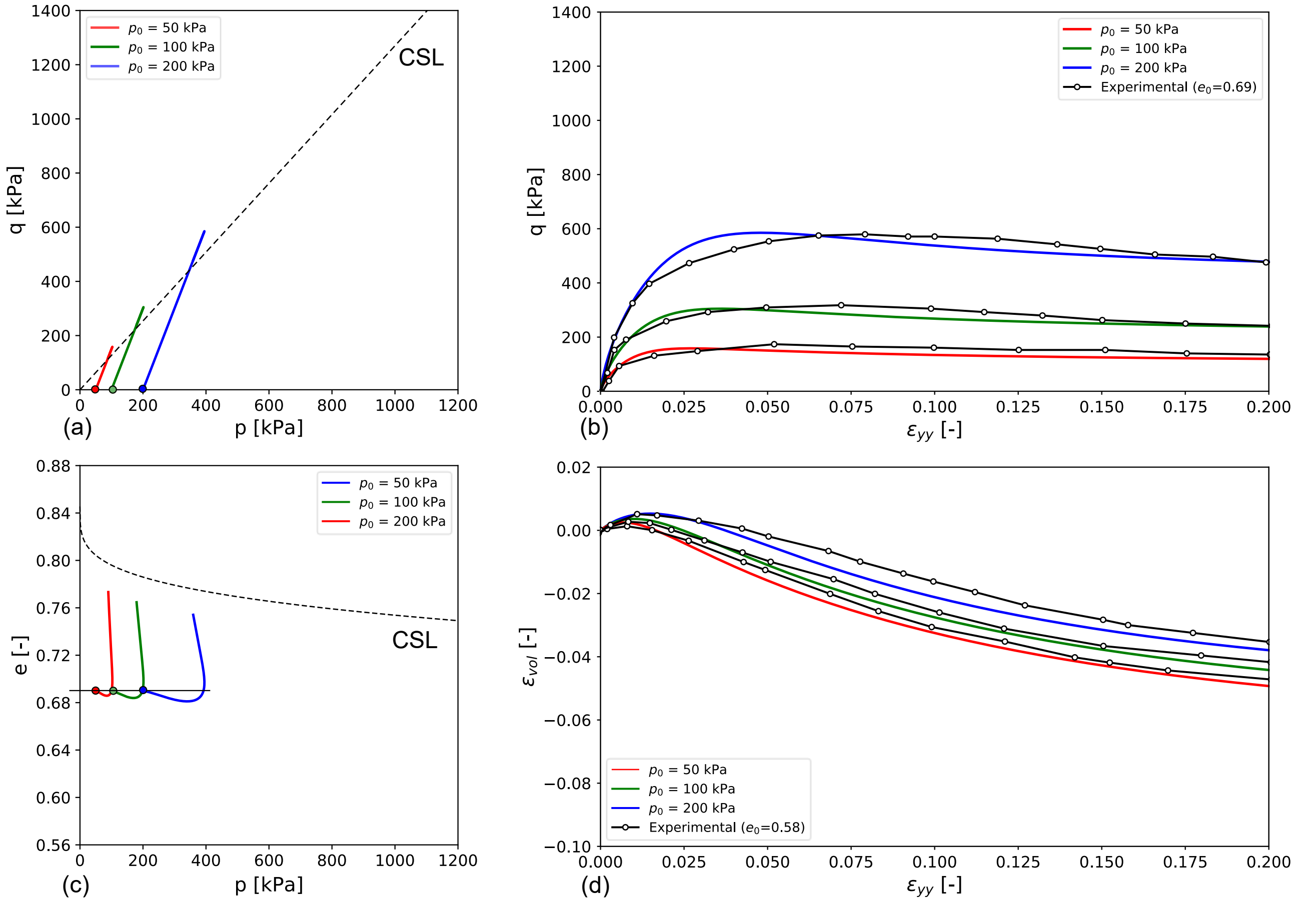

Figure 5-2 Monotonic drained triaxial tests on Karlsruhe sand for varying initial mean effective stress: comparison between experimental and numerical results.

To evaluate the model's ability to reproduce the influence of initial and loading conditions on the ratcheting, a series of stress-controlled one-way cyclic triaxial tests were simulated in SoilTest. These tests involved variations in asymmetry, amplitude, initial void ratio, and mean effective stress. In all the cases, the initial condition of the cyclic phase was reached through the p-constant stress path, as explained in paragraph 3.1.5.

Figure 5-3 presents an example of how solving the cyclic triaxial test described in Figure 3-5 using SoilTest. To simulate the stress path AB of Figure 3-5, the General tab of SoilTest needs to be utilised because the Cyclic Triaxial test tab only allows for a TX stress path during the monotonic loading phase. An initial void ratio $e_0 = 0.69$ and mean effective stress $p_0 = 200\ kPa$ are assumed in the initial isotropic state (Initial Phase).

Phase 1: Monotonic loading (p-constant stress path)

Phase 2: Loading branch of the cycle

Phase 3: Unloading branch of the cycle

Phase 4: Reloading branch up to the initial stress of the cycle

As mentioned in Chapter 4, instead of using the default number of steps (100), 30 steps are used per phase to compromise the amount of output data and the accuracy of the solution considering that a test characterised by relatively small load amplitude and very large number of cycles (10000) must be performed. Phases 1 to 4 will be repeated at 10000 to reproduce the experimental high-cycle test of Wichtrmann (2005).

A good practice to verify the correct setup of the input is to (first) run an individual loop and inspect the results. Figure 5-4 shows the results obtained with the setup of Figure 5-3. Consistency with Figure 3-5 (a) indicates the correct setup of the test. Additionally, the maximum q reached during the stress-controlled test is 210 kPa, much smaller than the monotonic strength (Figure 5-2). This confirms that 30 steps can be sufficient to obtain an accurate solution. The preliminary check also allows to exclude that, for an erroneous definition of the stress increment, the strength is mobilized during the stress-controlled test. Possible violation of the strength is more probable in tests aimed at the calibration of ζ (Figure 3-9).

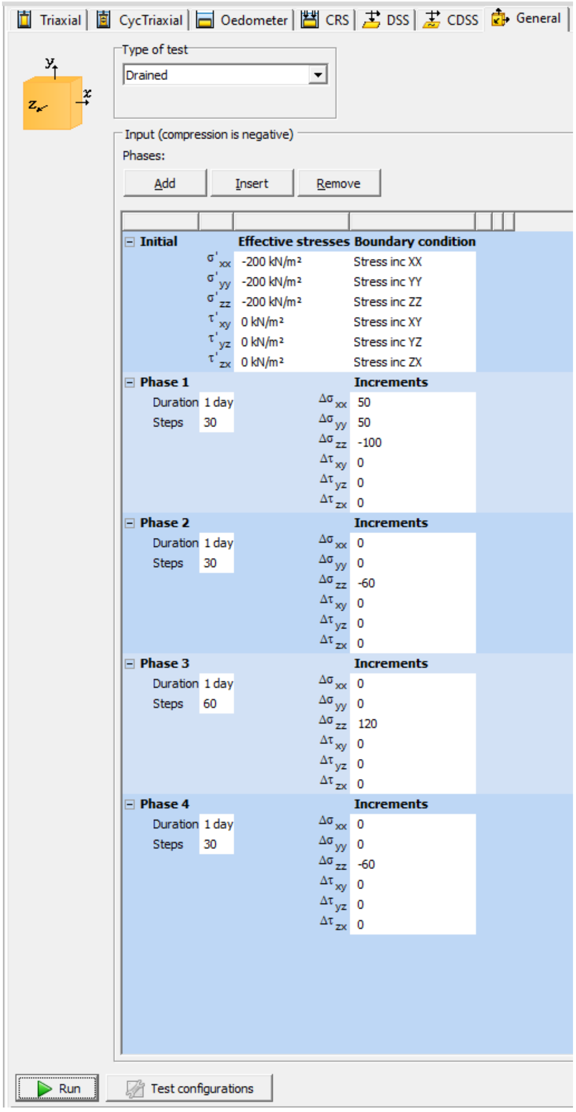

Figure 5-3 SoilTest General tab to perform a drained test characterized by an initial p-constant stress path and an individual cycle stress controlled triaxial.

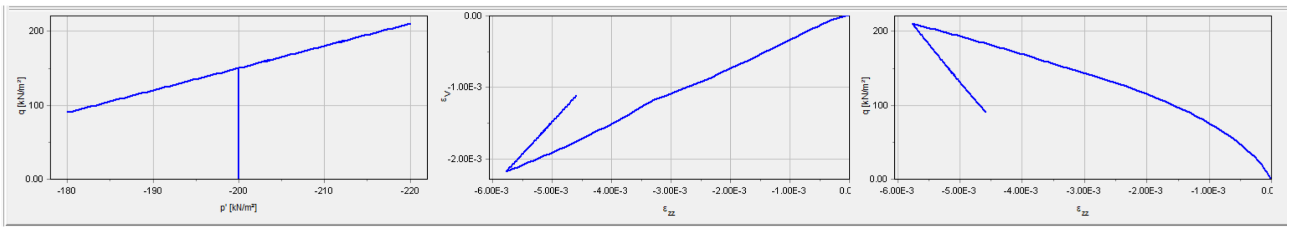

Figure 5-4 Results of the analysis

Figure 5-5 (top) shows the syntax of a new command available from the version 2023.02 in the command line of the General tab of PLAXIS SoilTest. The syntax requires specifying an interval of Phases among those defined in the GUI (Figure 5-3) and the number of times they should be repeated. Note that the Phase identification in the GUI and in the command line are not the same. In this example, the list 1 to 3 shown Figure 5-5 (top) refers to the interval of Phases from 2 to 4 in the GUI (Figure 5-3).

The Phases in the interval will be identified as a cycle. Figure 5-5 (bottom) shows results obtained after execution of the command and then pressing the run button. The output shows that, although no additional Phases are visualized in the GUI, a cyclic test (characterized by 10000 repetitions) has been performed.

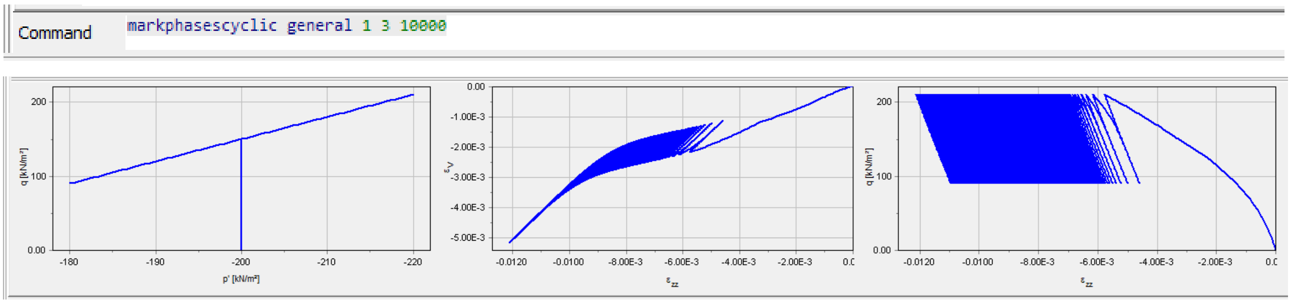

Figure 5-5 (top) New command available in the General tab to easily simulate cyclic tests characterized by high number of repetitions. (bottom) Results obtained when the new command is executed.

Figure 5-6 shows the syntax of a command that allows deleting the cyclic phases (deleting the repetition of the interval of Phases).

Figure 5-6 Useful command to delete the repetition of the Phases.

Figure 5-7 and Figure 5-8 show the total accumulated strain (Eq. 3-4) in a series of stress-controlled one-way asymmetric tests. The characteristics of sinusoidal cyclic loads are defined using two parameters, indicating the type and amplitude of the cycles. The stress amplitude ratio is defined as $\xi_c = \frac{q_{min}}{q_{max}}$, where q_{min} and q_{max} are the minimum and maximum loads reached during the test. Based on the value of ξ_c, four categories of cyclic loads can be defined. Two-way loads (loads crossing the zero) have $\xi_c < 0$. One-way loads when $\xi_c \geq 0$. Two-ways loads can be symmetric, in case of $\xi_c = -1$. One-way loads are asymmetric if $-1 < \xi_c < 0$; One-way symmetric loads are characterized by $\xi_c = 0$. $1 > \xi_c > 0$. The amplitude of cyclic loads is defined as $\xi_c = \frac{q^{ampl}}{q_{peak}}$ where q^{ampl} amplitude of the cyclic load and q_{peak} is the monotonic strength, which should be known before simulating the stress controlled cyclic tests. In this case, the cycles are described through: e_{ini} and p_{ini} $\Delta\eta$, η^{ave} considering the specific configuration of the laboratory tests (Paragraph 3.1.5).
The results are compared with the experimental data of Wicthman (2005) and simulations performed by Liu et al. (2019). Tests show the capability of SANISAND-MS to predict the effect of different factors on the amount of ratcheting accumulated by the Karlsruhe sand. Additional evidence about the capabilities of the model in reproducing laboratory tests is available in Liu et al. (2019) and Liu and Pisanò (2019).

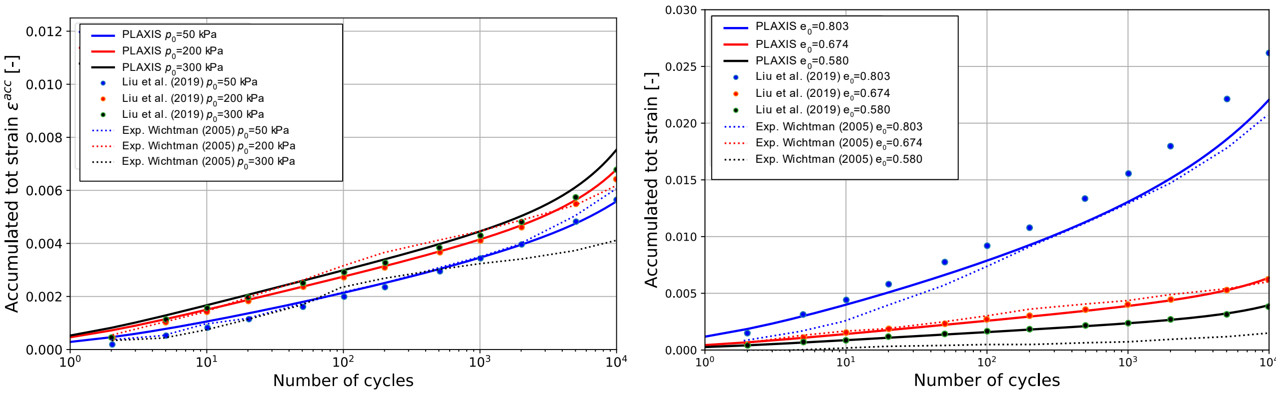

Figure 5-7 Influence of the initial mean effective stress and void ratio on cyclic strain accumulation in tests characterized by (left) $\mathrm{e}_{ini} = 0.684$, $\eta^{ave} = 0.75$ and $\Delta\eta = \frac{\Delta q}{p_{ini}} = 0.3$ and (right) $\mathrm{p}_{ini} = 200\ kPa$, $\eta^{ave} = 0.75$ and $\Delta\eta = \frac{\Delta q}{p_{ini}} = 0.3$, respectively.

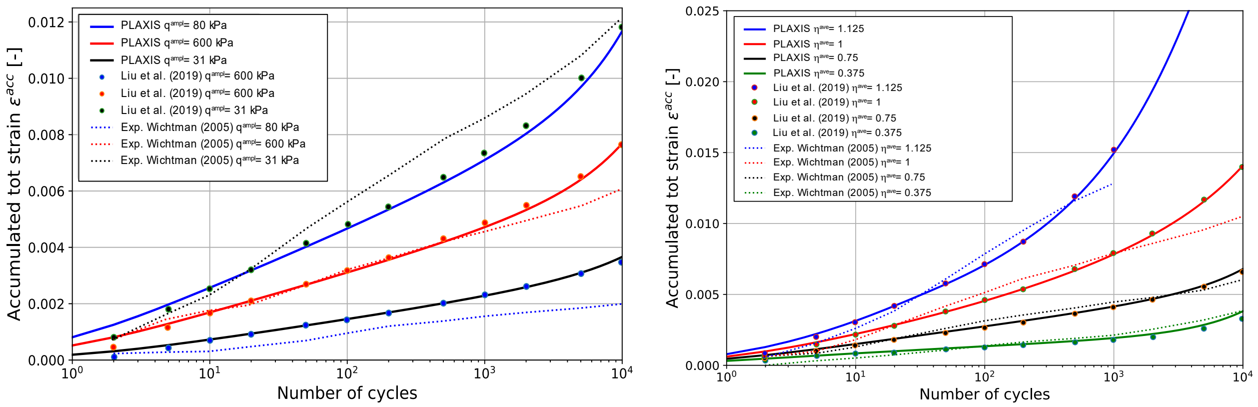

Figure 5-8 Influence of the load amplitude and stress ratio on cyclic strain accumulation in tests characterized by (left) $\mathrm{p}_{ini} = 200\ kPa$, $\mathrm{e}_{ini} = 0.702$, $\eta^{ave} = 0.75$ and (right) $\mathrm{p}_{ini} = 200\ kPa$, $\mathrm{e}_{ini} = 0.684$, $\Delta\eta = \frac{\Delta q}{p_{ini}} = 0.3$, respectively.

6.

Simulation of laterally loaded reduced-scale monopile tests with SANISAND-MS

To show the capabilities of the constitutive model implemented in PLAXIS 3D in simulating the soil-structure interaction, particularly in the context of monopile foundations for offshore wind turbines, two field tests conducted at the Dunkirk site on the laterally loaded reduced-scale monopiles, within PISA (PIle-Soil Analysis) project (Burd et al. 2019; Zdravković et al., 2019; Taborda et al. (2020); Byrne et al., 2020; Burd et al. 2020; McAdam et al., 2020), are reproduced in PLAXIS 3D.

The PISA project is a comprehensive pile testing programme that included ground characterization, field tests and FEM analyses aimed at developing a new design approach for large-diameter monopiles. In this example, one monotonic test (DM4) and one cyclic test (DM2) (Beuckelaers, 2017; Byrne et al., 2020; McAdam et al., 2020) conducted on piles with the same geometry (as listed in Table 6-1) and similar installation conditions are reproduced in PLAXIS 3D. The load-deflection curves obtained from these simulations are then compared with the experimental data to show the capability of SANISAND-MS in providing both qualitative and quantitative predictions of relevant aspects of the design of these foundations.
As depicted in Table 6-2, the cyclic tests consist in high-cyclic one-way tests in which five load packets with different amplitudes, LS, are sequentially applied. As mentioned earlier (with respect to laboratory tests in Paragraph 3.5), the amplitude of cyclic loads is defined as a percentage of the monotonic strength of the monopile. Therefore, a satisfactory prediction of the monotonic strength is a prerequisite for the consistent simulation of the cyclic phases. In this example, the monotonic strength of the pile is evaluated through a push-over analysis where the displacement is applied at the top of the monopile. For the cyclic tests, 100 cycles are simulated for each of the first four load parcels, while 6 cycles are simulated for LS5. As mentioned in Paragraph 4, cyclic analyses of monopiles can be performed through two alternative equivalent procedures:

- Dynamic calculations, which are easier for Phase settings of the calculations but might require more computation time when $\xi_b \geq 25\%$;
- A sequence of static phases, which could necessitate the creation of a large number of phases to represent the loading and reloading branches of the cycles. This procedure can be facilitated by the PLAXIS python scripting.

In this example, both procedures are used. LS1 and LS2 are simulated thorough dynamic analysis. For LS3, LS4 and LS5, (Table 6-2) the calculations are performed with a sequence of plastic phases which, providing essentially similar results, considerably reduce the calculation time compared with dynamic calculations.

Table 6-1 PISA PILE tests reproduced in PLAXIS 3D

Test	Type	Diameter D (m)	Embedment L (m)	Eccentricity h (m)	Aspect ratio L/D	Thickness t (mm)	Eccentricity ratio h/D
DM4	monotonic	0.762	3.99	10	5.24	14	13.12
DM2	cyclic	0.762	3.99	10	5.24	14	13.12

Table 6-2 Cyclic load set applied to the monopile DM2.

Load set (LS)	Maximum Load, F_{max} (kN)	ζ_b	ζ_c	Number of cycles	Number of cycles symulated
1	10	0.046	0	5100	100
2	20	0.093	0	3300	100
3	40	0.19	0	8100	100
4	80	0.37	0	11110	100
5	160	0.74	0	31	10

Figure 6-1 shows the geometry of the 3D model. Half of the geometry is modelled, exploiting the symmetry of the problem. To facilitate a comparison of the results with existing literature, the subsoil model of the Dunkirk site employed by Taborda et al. (2020) is adopted in this study to define the initial stress and hydraulic conditions in the 3D finite element model. Soil deposit is characterized by a sand layer extended from 3 down to 30 m and a dense upper fill layer. As shown in Figure 6-2 (a) and (b), the groundwater table is located at 5.4 m below the ground surface, so the conditions of the very dense and partially saturated fill layer may have likely affected the pile test results and should be considered in the FE simulation. Due to the lack of more detailed information, as done by Taborda et al. (2020), the mechanical properties assumed for the 3m-thick upper dense layer (Figure 6-2) as those adopted for the underlying sand deposit. The higher strength of the material is accounted for indirectly through the modelling of the suction type pore pressures.

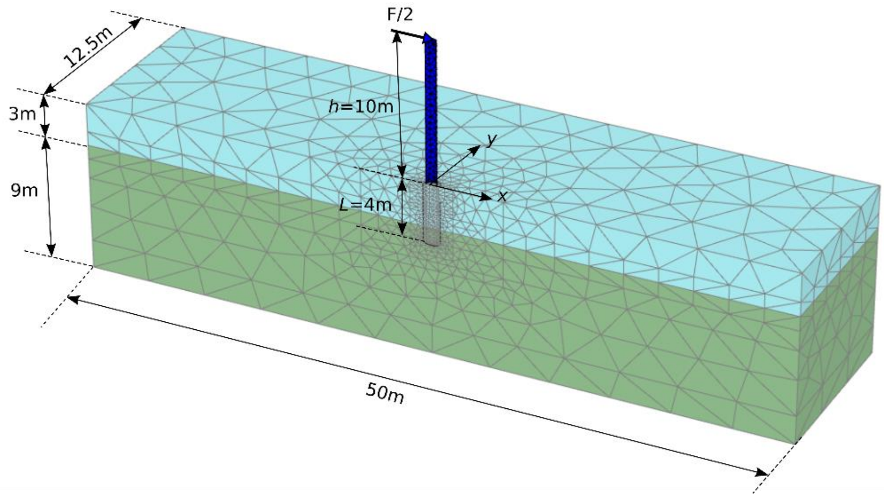

Figure 6-1 3D FE model.

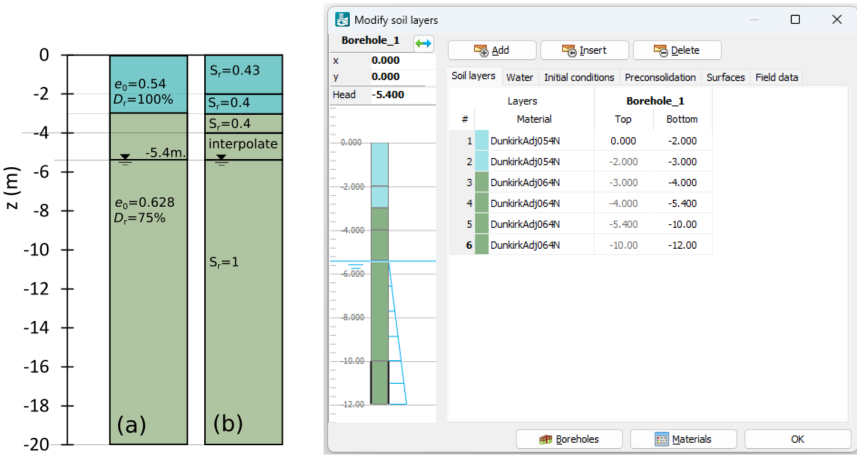

Figure 6-2 Discretization for the mechanical properties (material sets). (b) Discretisation used for the saturation and water conditions.

The only difference between the mechanical properties of the two material set assigned to the layers consists of the initial void ratio (Figure 6-2 (a)), with $e_0 = 0.54$ (corresponding to a $D_r = 100\%$) being adopted for the upper fill layer, while $e_0 = 0.628$ is considered for the underlying sand deposit. The model parameters are summarised in Table 6-3.The soil unit weight is assumed as $\gamma_{unsat} = 17.1\mathrm{kN/m^3}$ and $\gamma_{sat} = 19.9\mathrm{kN/m^3}$.

Table 6-3 Dunkirk sand based on in situ tests.

PARAMETER	SYMBOL	VALUE	UNITS
Shear modulus coefficient	G_0	451.5	-
Poisson's ratio	υ	0.17	-
Stress ratio at critical state in triaxial compression	M_c	1.28	-
Ratio between critical stress ratios in triaxial extension and compression	c	0.7188	-
Slope of the CSL in the compressibility plane	λ_c	0.135	-
Void ratio of the CSL at p=0kPa	e_0	0.91	
Critical state line constant	ξ	0.179	-
Size of the yield surface	m	0.065	-
Hardening parameter	h_0	3.5	-
hardening parameter	c_h	1	-
Bounding parameter	n^b	1.9	-
Dilatancy parameter	A_o	1.3	-
Dilatancy surface parameter	n^d	0.75	-
MS parameter	μ_0	260	-
MS parameter	ζ	0.0001	-
MS parameter	β	1	-
Initial void ratio of the layer	e_{ini}	Varies: 0.54 / 0.628	-
Maximum void ratio	e_{max}	0.91	-
Minimum void ratio	e_{min}	0.54	-
Maximum bounding stress ratio in triaxial compression	$M^{b,max}$	1.63	-
Toggle	Elscheme	0	-

To model the active pore pressure profile assumed in Taborda et al. (2020), it is convenient to sub-divide the soil domain in five layers as shown in Figure 6-2 (b) while keeping the same set of model parameters. In Figure 6-2 (a) and (b) the colours recall the material set, in Figure 6-2 (b) the saturation degree and water conditions assumed in each sublayer are shown. The pore pressure profile is obtained by maintaining the default ground water properties in the “groundwater” tab of the “material sets” window, and by specifying the degree of saturation for each layer (Figure 6-2). After selecting the soil clusters of the layer, the Saturation can be specified in the “Model explorer”, under the “WaterConditions”: $S_r = 0.43$ for $z = [0; -2\ m]$, $S_r = 0.4$ for $z = [-2; -3\ m]$ and $S_r = 0.4$ for $z = [-3; -4\ m]$. Moreover, the option interpolate (for the pore pressures) is chosen for the layer located in $z = [-4; -5.4\ m]$ (between the saturated zone and the unsaturated layer with constant suction). Lastly, below the water level, the pore pressures follow a hydrostatic distribution with $\gamma_w = 10\ \mathrm{kN/m^3}$.

The geometry of the pile is characterized by an outer diameter of $D = 0.762\ \mathrm{m}$, an embedded length of $L = 4\ \mathrm{m}$, a thickness of $t = 14\ \mathrm{mm}$. The load (or displacement) eccentricity is considered $h = 10\mathrm{m}$. The unit weight of the monopile is assumed as $\gamma = 0\mathrm{kN/m^3}$, having modest influence on the results of lateral analyses. By using plate elements to model the monopile and by assuming an isotropic behaviour, the other properties necessary to model the monopile are $E_1 = 210\ 000\ \mathrm{kN/m^2}$, $\upsilon_{12} = 0.3$ and $d = t$.

To simulate the applied loads and displacements, a “point load” and “point prescribed displacement” should be respectively created at the head of the pile (in the Structures mode). Alternatively, also a line load or displacement can be defined.

The mesh in Figure 6-1 comprises 10-node tetrahedral elements and is refined around the pile surface. Zero-thickness interface elements are used to simulate the interaction between the soil and the monopile plate elements. Note that in PLAXIS, the constitutive model used for the interface element is always characterised by an elastoplastic Mohr-Coulomb constitutive model. In this case, a “direct stiffness determination” option is chosen in the Interface Tab of the Soil User Defined Material. For the interface, normal (k_n) and shear (k_s) stiffnesses are both set to $10E5\ kN/m^3$, while a friction angle of $32°$ (Taborda et al., 2020) and cohesion of $0.1\ kPa$ are chosen. Two structural nodes are pre-selected at the mudline level: node A, (X=+0.381 m, Y=0 m, Z=0 m) and node B, (X=−0.381 m, Y=0 m, Z=0 m).

The simulations of the monotonic and cyclic tests are performed thorough several phases:

- Step1: an initial phase with calculation type set to “K_0-*procedure*”; note that a $K_0 = 0.4$ was assumed for the two sand deposits
- Step2: a plastic loading phase in which the interfaces and structural elements are activated
- Step3a: a plastic loading phase where a point (or line) displacement is applied at the top of the monopile to achieve a target displacement of $0.1D$ at the ground-surface
- Step3b: plastic loading or dynamic phases in which the cyclic load scenario is applied.

Monotonic calculation will require the sequence Step 1 → 2 → 3a, whereas the sequence Step 1 → 2 →3b are needed for cyclic calculations (Figure 6-3).

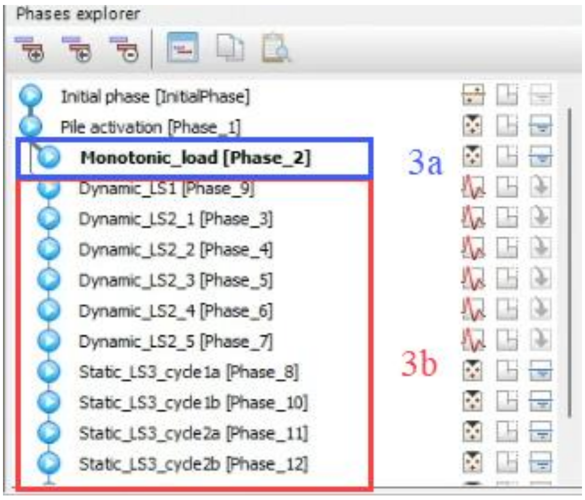

Figure 6-3 Sequence of Phases used in this example.

The load multiplier assigned to the X component of dynamic load was specified through a table where F_x varies between the amplitude of the load set and 0. Considering the symmetry of the problem, half of the load in Table 6-2 is applied in the 3D model. In both cases, the period is $\mathrm{T} = 500\ s$ ($\mathrm{f} = 0.002\ s^{-1}$). The frequency was iteratively determined until the accelerations in the soil domain becomes small enough to be disregarded. The sampling time interval is $dt = 250\ \mathrm{s}$. To simulate the load set LS1, in the Phase window, the following settings are assigned: $dynamic\ \mathrm{time\ interval} = 50000\ s$ (to run 100 cycles), $Max\ steps = 5000\ Number\ of\ sub\ steps = 2$ (to use a $dt = 10\ \mathrm{s}$). The 100 cycles of the load set LS2 are performed in 5 phases (Figure 6-3). For every phase: $dynamic\ \mathrm{time\ interval} = 10000s$ (to run 20 cycles), $Max\ steps = 2000$ and $Number\ of\ sub\ steps = 2$ (to use a $dt = 2.5\ \mathrm{s}$). For the plastic phases used to simulate the loading and unloading stages of the cyclic set LS3, a maximum load fraction per step of 0.01 is defined. It will be seen that the displacements predicted for LS2 and LS3 are overestimated, consequently, LS4 and LS5 are not simulated at this stage of the exercise.

For the push-over analysis (Phase 3a), the default settings are used.

Figure 6-4 shows the monotonic load-deflection curve obtained from the push-over analysis. The Total displacement Ux of the preselected node A is plotted against the F (or Fx). In Figure 6-4, the dashed line represents the later response computed in PLAXIS 3D in the hypothesis of wished-in places pile.

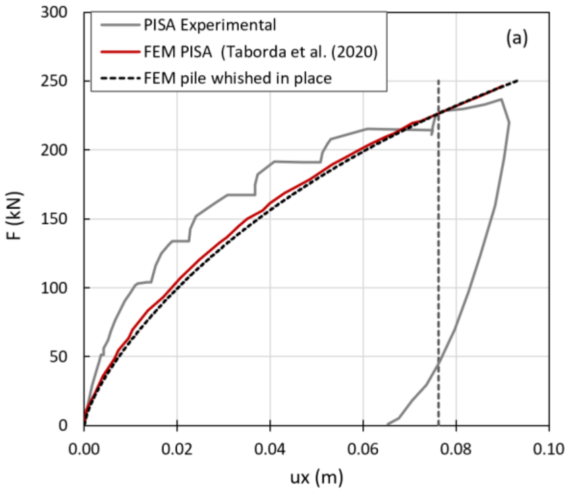

Figure 6-4 Monotonic lateral load response of the pile: obtained in this example, experimental data and numerical results of the 3D FE analysis of Taborda et al. (2020).

To elaborate the results of dynamic phases, the dynamic time against the Total displacement Ux of the preselected right hand side node of the pile is extracted in output. The force applied at the top of the pile (at every time instant) can be computed from the “Dynamic time”, by knowing the maximum force applied in every cycle (Table 6-2) and frequency of the input load multiplier. To elaborate the results of plastic phases, the Total displacement Ux of the preselected right hand side node of the pile, against the $\sum Mstage$ of the Project can be extracted in output. In this case, the horizontal force at every step can be calculated multiplying $\sum Mstage$ by the respective F_{max} of the load parcel (Table 6-2).

In Figure 6-5 (b), the relative displacement has been computed as

$$U_{rel} = U_{x,max}^{i} - U_{x,max}^{1} \qquad \textit{Eq. 6-1}$$

Where $U_{x,max}^{i}$ is the displacement of the node at the peak of the force in the i-th load-cycle of the set and $U_{x,max}^{1}$ the displacement at the peak of the first cycle.

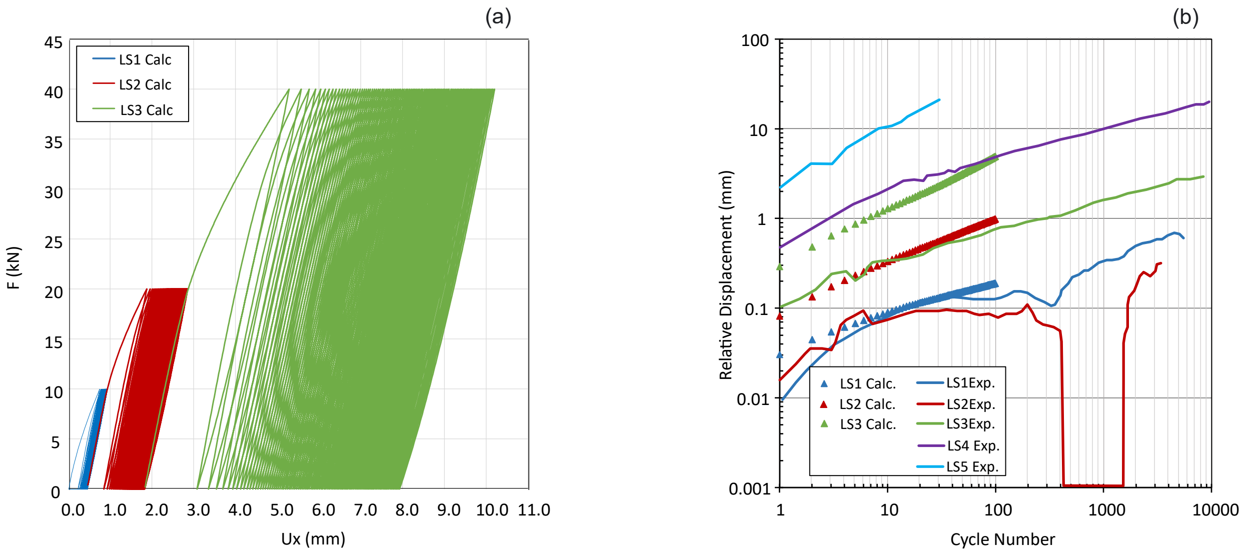

Figure 6-5: Numerical results obtained with wished-in-place pile assumption: (a) Cyclic lateral load response (for node A) during the sequential simulation of 100 cycles of LS1, LS2, and LS3. (b) Accumulated relative displacement for the load packets LS1, LS2, LS3, compared with the experimental data from Byrne et al. (2020).

By extracting the Total displacement Uz for the preselected pile nodes, A and B, the rigid rotation of the pile can be approximated as $\psi^i_{max} = \text{degrees}\ (atan\left(\left(U^i_{z,max}\right)_{DX} - \left(U^i_{z,max}\right)_{SX}\right)/D)$. The accumulated relative rotation can be computed as in Beuckelaers (2017):

$$\bar{\psi}_{acc} = \frac{\psi^i_{max} - \psi^1_{max}}{2^\circ} \qquad \textit{Eq. 6-2}$$

Where accumulated rotation is normalised by the value considered as the rotation correspondent to ultimate limit state (ULS).

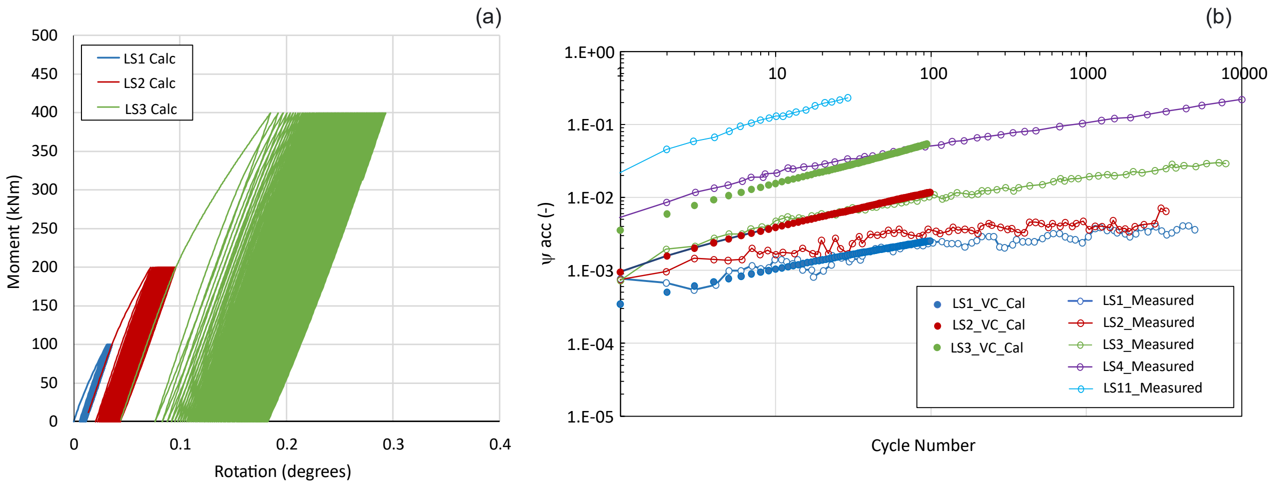

Figure 6-6 Numerical results obtained with wished-in-place pile assumption: (a) rotation of the pile during the sequential simulation of 100 cycles of LS1, LS2, and LS3. (b) accumulated rotation for the load packets LS1, LS2, LS3, compared with the experimental data from Beuckelaers (2017).

The installation effects associated with typical impact pile driving can be modelled with the simplified procedure of applying a positive volumetric strain or prescribed displacement (Broere and Van Tol, 2006). In this section, the calculations are repeated after the simulation of a volumetric strain of the soil plug, performed before the activation of the interfaces and structural elements (before Step 1). In the additional Phase (Step 1b) positive strains are imposed in X and Y to the cluster of elements inside the pile directions, $\varepsilon_{vol} = \varepsilon_x + \varepsilon_y$ because it has been noticed that the strains in the vertical direction Z have little effect on pile response. A total volumetric strain of 1% is applied in this case. The results of the simulations are shown in Figure 6-7, Figure 6-8 and Figure 6-9.

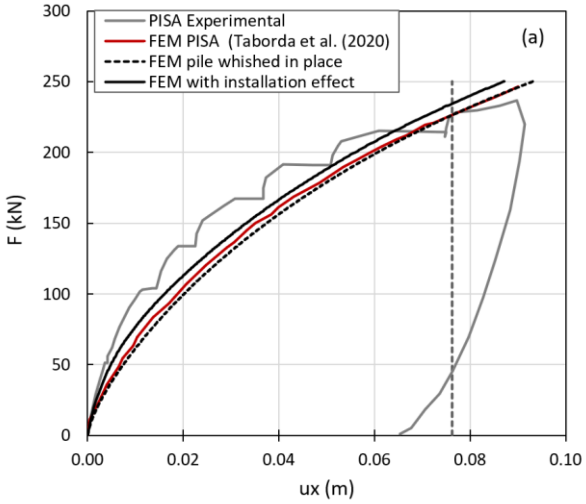

Figure 6-7 Monotonic lateral load response of the pile: obtained in this example (black lines), experimental data (grey), and numerical results of the 3D FE analysis of Taborda et al. (2020) (red).

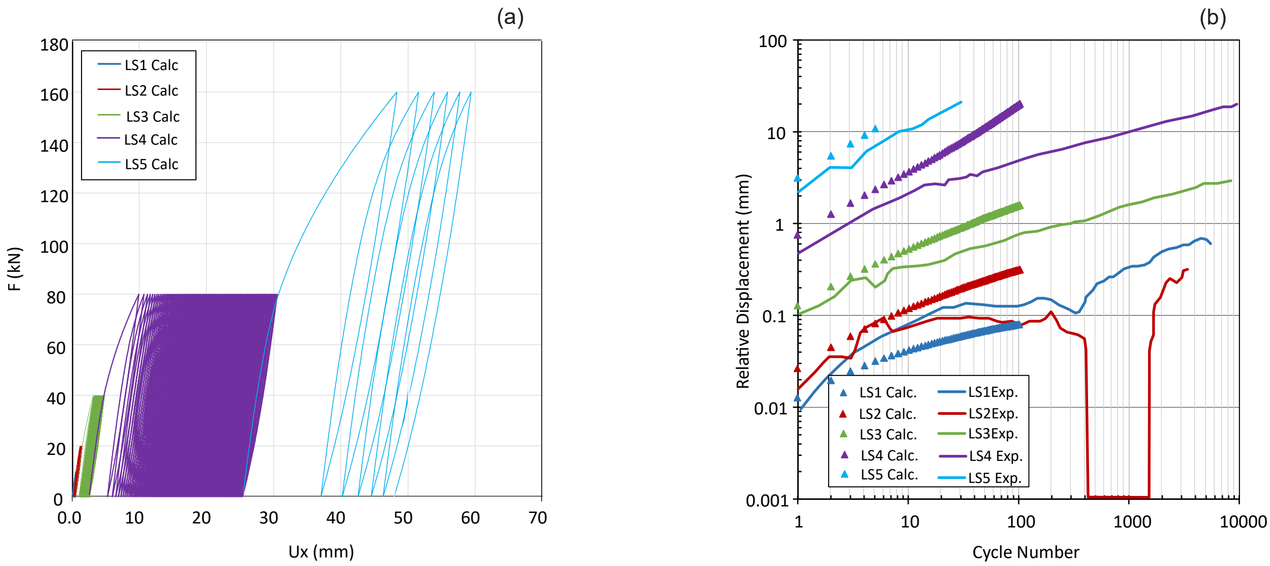

Figure 6-8 Numerical results obtained when the effect of the installation is accounted for via simplified procedure: (a) lateral displacement of node A , and (b) accumulated relative displacement compared with the experimental data from Byrne et al. (2020).

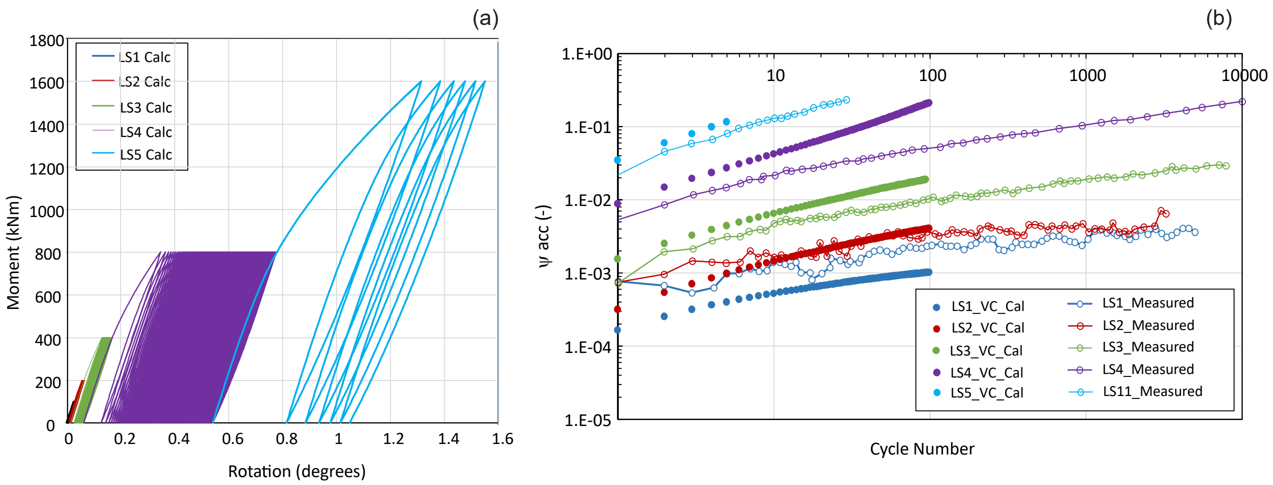

Figure 6-9 Numerical results obtained when the effect of the installation is accounted for via simplified procedure: (a) rotation, and (b) accumulated relative rotation compared with the experimental data from Beuckelaers (2017)

Conclusions:

-The monotonic strength of the pile (Figure 6-4 and Figure 6-7) is satisfactorily predicted in both cases (wished-in-place pile and considering the effect of installation).

-When the effect of the installation is considered, the SANISAND-MS (with the same set of parameters) reproduces a stiffer lateral response of the pile at early load stages. The increase in lateral stiffness improves the prediction of the accumulated relative displacements and rotation of the pile (Figure 6-8 and Figure 6-9 in comparison with Figure 6-5 and Figure 6-6).

-For the illustrative purpose of this manual, the experimental load history is not fully reproduced. For the number of cycles simulated, except for LS4, the model seems to capture the rate of accumulation of relative displacements and rotations and its dependency on the load amplitude. When the wished-in-places hypothesis is assumed, the magnitude of the relative displacement is considerably over-estimated. When installation effects are considered (Figure 6-8 and Figure 6-9) an improved agreement with the experimental results is observed especially for the displacement/rotation predicted for the first loop of every load packet, which is in line with experimental evidence, which related the amount of the relative tilt and lateral displacement with the initial stiffness of the pile.

-An improved prediction of the rate of displacements and rotation accumulation can be obtained by adopting a better calibration of the ratcheting parameters (ζ and μ_0).

7.

References

Abadie, C.N., Byrne, B.W., Houlsby, G.T., (2017). Modelling of monopile response to cyclic lateral loading in sand. Offshore Site Investigation Geotechnics 8th International Conference Proceedings 1046–1053. https://doi.org/10.3723/osig17.1046

Abadie, C.N., Beuckelaers, W.J.A.P, Byrne, B.W., Houlsby, G.T., Burd, H.J., McAdam, R.A., (2023) Modelling Lifetime Performance of Monopile Foundations for Offshore Wind Applications Journal of Geotechnical and Geoenvironmental Engineering, 149(9), https://doi.org/10.1061/JGGEFK.GTENG-9833

API. (2000). Recommended Practice for Planning, Designing and Constructing Fixed Offshore Platforms—Working Stress Design.

Been, K. & Jefferies, M. G. (1985). A state parameter for sands. *Géotechnique* 35, No. 2, 99–112, https://doi.org/10.1680/geot.1985.35.2.99

Been, K. & Jefferies, M. G. (2004). Stress-dilatancy in very loose sand. Canadian Geotechnical Journal 41: 972-989

Beuckelaers, W. J. A. P. (2017). “Numerical Modelling of Laterally Loaded Piles for Offshore Wind Turbines.” DPhil Thesis, University of Oxford.

Byrne, B.W., McAdam, R.A., Beuckelaers, W.J.A.P., Burd, H.J., Gavin, K., Houlsby, G.T., Igoe, D.J.P., Jardine, R., Martin, C.M., Authors, M., (2020). Cyclic Laterally Loaded Medium Scale Field Pile Testing for the PISA Project, in: Proceedings Fourth International Symposium on Frontiers in Offshore Geotechnics. pp. 1323–1332

Broere, W., Van Tol, A.F., (2006). Modelling the bearing capacity of displacement piles in sand. Proc. Inst. Civ. Eng. Geotech. Eng. 159, 195–206. https://doi.org/10.1680/geng.2006.159.3.195

Burd, H.J., Beuckelaers, W.J.A.P., Byrne, B.W., et al. (2019). New data analysis methods for instrumented medium scale monopile field tests. Géotechnique doi:10.1680/jgeot.18.pisa.002

Burd, H.J., Taborda, D.M.G., Zdravkovic, L., et al. (2020). PISA design model for monopiles for offshore wind turbines: Application to a marine sand. Géotechnique doi:10.1680/jgeot.18.p.277

Corti, R. (2016). Hardening memory surface constitutive model for granular soils under cyclic loading conditions (Doctoral dissertation, University of Bristol).

Corti, R., Diambra, A., Wood, D. M., Escribano, D. E., & Nash, D. F. (2016). Memory surface hardening model for granular soils under repeated loading conditions. *Journal of Engineering Mechanics*, 142(12), 04016102.

Dafalias, Y. F., & Manzari, M. T. (2004). Simple plasticity sand model accounting for fabric change effects. *Journal of Engineering mechanics*, 130(6), 622-634.

Escribano DE. (2014) Evolution of stiffness and deformation of Hostun Sand under drained cyclic loading. PhD thesis. UK: University of Bristol;.

Houlsby, G.T., Abadie, C.N., Beuckelaers, W.J.A.P., Byrne, B.W., (2017). A model for nonlinear hysteretic and ratcheting behaviour. International Journal of Solids and Structures 120. https://doi.org/10.1016/j.ijsolstr.2017.04.031

Jefferies, M. and Been, K. (2016). Soil Liquefaction, a Critical State Approach. Applied geotechnics series. CRC Press.

Li, Z., Liu, H., Hicks, M. A. & Pisanò, F. (2023). Influence of static–cyclic load misalignment on the drained tilting response of offshore monopiles in sand. Computers and Geotechnics 156, 105306 https://doi.org/10.1016/j.compgeo.2023.105306

Loukidis, D., and Salgado, R. (2009). “Modeling sand response using two-surface plasticity.” *Comput. Geotech*., 36(1-2), 166–186

Liu, H. Y., Abell, J. A., Diambra, A., & Pisanò, F. (2019). Modelling the cyclic ratcheting of sands through memory-enhanced bounding surface plasticity. *Géotechnique*, 69(9), 783-800.

Liu, H. Y., & Pisanò, F. (2019). Prediction of oedometer terminal densities through a memory-enhanced cyclic model for sand. Géotechnique Letters, 9(2), 81-88.

Liu, H., Kementzetzidis, E., Abell, J. A. & Pisanò, F. (2022a). From cyclic sand ratcheting to tilt accumulation of offshore monopiles: 3D FE modelling using SANISAND-MS. G´eotechnique 72, No. 9,

753–768.

Liu, H., Pisanò, F., Jostad, H. P. & Sivasithamparam, N. (2022b). Impact of cyclic strain accumulation on the tilting behaviour of monopiles in sand: An assessment of the Miner’s rule based on SANISAND-MS 3D FE modelling. Ocean Engineering 250,110579.

McAdam, R.A., Byrne, B.W., Burd, H.J., Beuckelaers, W.J.A.P., Gavin, K.G., Houlsby, G.T., Igoe, D.J.P., Jardine, R.J., Martin, C.M., Muirwood, A., Potts, D.M., Gretlund, J.S., Taborda, D.M.G., Zdravkovic, L., (2020). Monotonic laterally loaded pile testing in a dense marine sand at Dunkirk. Geotechnique 70, 986–998. https://doi.org/10.1680/jgeot.18.PISA.004

Shibuya S, Park C-S, Tatsuoka F, Abe F, Teachavorasinskun S, Kohata Y, Sato T. The significance of local lateral-strain measurement of soil specimens for a wide range of strain. *Soils Found* 1994;34(2):95–105

Taborda, D.M.G., Zdravkovic, L., Potts, D.M., Burd, H.J., Byrne, B.W., Gavin, K.G., Houlsby, G.T., Jardine, R.J., Liu, T., Martin, C.M., McAdam, R.A., (2020). Finite-element modelling of laterally loaded piles in a dense marine sand at Dunkirk. Geotechnique 70, 1014–1029. https://doi.org/10.1680/jgeot.18.PISA.006

Taiebat, M. and Dafalias Y.F. (2008). SANISAND: Simple anisotropic sand plasticity model. Int. J. Numer. Anal. Meth. Geomech.. (32) https://doi.org/10.1002/nag.651 Tatsuoka F, Ishihara K. Drained deformation of sand under cyclic stresses reversing direction. Soils Found 1974;14(3):51–65.

van Eekelen, H.A.M, (1980). Isotropic yield surfaces in three dimensions for use in soil mechanics. International Journal for numerical and analytical methods in geomechanics. 4,89-101 https://doi.org/10.1002/nag.1610040107

Verdugo R, Ishihara K. (1996) The steady state of sandy soils. Soils and Foundations; 36(2):81–91.

Zdravković, L., Jardine, R.J., Taborda D.M.G., et al. (2019a). Ground characterisation for PISA pile testing and analysis. Géotechnique doi:10.1680/jgeot.18.pisa.001

Wichtmann, T. (2005a). Explicit accumulation model for non-cohesive soils under cyclic loading (Doctoral dissertation, Inst. für Grundbau und Bodenmechanik).

Wichtmann, T., Niemunis, A., & Triantafyllidis, T. (2005b). Strain accumulation in sand due to cyclic loading:drained triaxial tests. *Soil Dynamics and Earthquake Engineering*, 25(12), 967-979.

Wichtmann, T., Niemunis, A., & Triantafyllidis, T. (2007). Strain accumulation in sand due to cyclic loading: drained cyclic tests with triaxial extension. *Soil Dynamics and Earthquake Engineering*, 27(1), 42-48.

Wichtmann, T., Niemunis, A., & Triantafyllidis, T. (2010). Strain accumulation in sand due to drained cyclic loading: on the effect of monotonic and cyclic preloading (Miner's rule). Soil Dynamics and Earthquake Engineering, 30(8), 736-745.

Wichtmann, T. (2016). Soil behaviour under cyclic loading-experimental observations, constitutive description and applications. Th. Triantafyllidis.

APPENDIX

A: Notation and basic elastoplastic equations

Throughout the manual, tensor quantities are denoted with boldface characters in a direct notation. Stress and strain tensors are decomposed in an isotropic and a deviatoric part. The symbol $\boldsymbol{\sigma}$ indicates the stress tensor, the mean effective stress is

$$p = \frac{1}{3}\, tr(\boldsymbol{\sigma}) \qquad \text{Eq. A-1}$$

and the deviatoric stress tensor and the von Mises equivalent stress are, respectively:

$$\boldsymbol{s} = \boldsymbol{\sigma} - p\boldsymbol{I}, \qquad q = \sqrt{\frac{3}{2}} \cdot |\boldsymbol{s}| \qquad \text{Eq. A-2}$$

The symbol $\boldsymbol{I}$ represents the second-order identity tensor ($\boldsymbol{I} = \delta_{ij}$, δ_{ij} being the Kronecker's symbol) and the symbol "**:**" is used to indicate the inner product between tensors (i.e. $\boldsymbol{s}{:}\,\boldsymbol{s} = s_{ij}s_{ij}$.) through which it is possible to define the Euclidean norm $|\boldsymbol{s}| = \sqrt{\boldsymbol{s}{:}\,\boldsymbol{s}}$. To characterise the hardening mechanism and the plastic flow of the model, the deviatoric stress ratio $\boldsymbol{r}$ tensor and the related norm η (i.e. the stress ratio) are defined respectively as

$$\boldsymbol{r} = \frac{\boldsymbol{s}}{p}, \qquad \eta = \sqrt{\frac{3}{2}} \cdot |\mathbf{r}|\,. \qquad \text{Eq. A-3}$$

Similarly, the strain tensor $\boldsymbol{\varepsilon}$ can be decomposed into the volumetric strain

$$\varepsilon_v = \varepsilon_{xx} + \varepsilon_{yy} + \varepsilon_{zz} \qquad \text{Eq. A-4}$$

and the deviatoric strain tensor $\boldsymbol{e}$

$$\boldsymbol{e} = \boldsymbol{\varepsilon} - \frac{\varepsilon_v}{3}\boldsymbol{I}. \qquad \text{Eq. A-5}$$

In what follows, all stress measures are considered as effective and, for the sake of simplicity, the superscript " ′ ", commonly used in soil mechanics notation, is omitted. Furthermore, the symbol " $\dot{}$ " is used to denote incremental quantities.

The Lode angle equation used in the following sections results in $\theta = 0°$ at triaxial compression and $\theta = 60°$ at triaxial extension.

$$cos(3\theta) = \frac{3\sqrt{3}}{2}\,\frac{J_{3D}}{\sqrt[2]{(J_{2D})^3}} \qquad \text{Eq. A-6}$$

where:

$$J_{2D} = \frac{1}{2}\boldsymbol{s}{:}\,\boldsymbol{s} \qquad \text{Eq. A-7}$$

$$J_{3D} = \frac{1}{3}\mathbf{s}:\mathbf{s}:\mathbf{s} \; = \; det\,\mathbf{s}$$ *Eq. A-8*

The main set of constitutive equations often required to characterize an elastoplastic material are recalled hereafter:

1. Hypothesis of strain additivity:

$$\dot{\boldsymbol{\varepsilon}} = \dot{\boldsymbol{\varepsilon}}^{el} + \dot{\boldsymbol{\varepsilon}}^{pl}$$ *Eq. A-9*

2. Yield surface:

$$f(\boldsymbol{\sigma}, \boldsymbol{q}) = 0$$ *Eq. A-10*

3. Elastic relationship between elastic strain rate and stress rate:

$$\dot{\boldsymbol{\sigma}} = \boldsymbol{D}^e \cdot \dot{\boldsymbol{\varepsilon}}^{el}$$ *Eq. A-11*

4. Flow rule:

$$\dot{\boldsymbol{\varepsilon}}^{pl} = \langle L \rangle \boldsymbol{R}$$ *Eq. A-12*

5. Hardening rule

$$\dot{\boldsymbol{q}} = \langle L \rangle \overline{\boldsymbol{q}}$$ *Eq. A-13*

Following the standard form, $\dot{\boldsymbol{\varepsilon}}^{el}$ and $\dot{\boldsymbol{\varepsilon}}^{pl}$ indicate the increments of the elastic and plastic parts of the strain tensor, $\boldsymbol{q}$ generically designates a set of hardening variables, the symbol L stands for the plastic multiplier or loading index, $\boldsymbol{R}$ is the derivative of the plastic potential with respect to the current stress state, $\boldsymbol{D^e}$ is the elastic stiffness matrix and $\dot{\boldsymbol{q}}$ is the rate of the vector of hardening variables. The equations listed in $\overline{\boldsymbol{q}}$ can be tensor valued or scalar valued depending on the tensorial order of $\boldsymbol{q}$. $\langle \cdot \rangle$ denotes the Macaulay brackets.

The elastoplastic stiffness matrix $\boldsymbol{D}^{ep}$ which relates the increments of stress and total strain (i.e. $\dot{\boldsymbol{\sigma}} = [\,\boldsymbol{D^{ep}}\,]\dot{\boldsymbol{\varepsilon}}$), is obtained by substituting the additivity and the flow rule into the incremental stress-elastic strain relationship

$$\boldsymbol{D}^{ep} = \boldsymbol{D}^e - \langle L \rangle \boldsymbol{D}^e \boldsymbol{R},$$ *Eq. A-14*

with L the plastic multiplier. L can be explicitly obtained by satisfying the consistency condition $\dot{f}(\boldsymbol{\sigma}, \boldsymbol{q}) = 0$

$$L = \left[\frac{(\mathbf{D}^e \boldsymbol{L})^T}{K_P + (\boldsymbol{D}^e \boldsymbol{R})\boldsymbol{L}^T}\right]\dot{\boldsymbol{\varepsilon}}$$ *Eq. A-15*

In Eq. A-15, $\boldsymbol{L}$ represents the gradient $\partial f / \partial \sigma_{ij}$ and K_P the plastic modulus defined as

$$K_p = -\left(\frac{\partial f}{\partial \boldsymbol{q}}\right)\overline{\boldsymbol{q}}\,.$$ *Eq. A-16*

By substituting Eq. A-15 into Eq. A-14 it is possible to rewrite the expression of the elastoplastic stiffness matrix in its final form as

$$\boldsymbol{D^{ep}} = \left[\boldsymbol{D}^e - \frac{(\boldsymbol{D}^e \boldsymbol{R})(\boldsymbol{D}^e \boldsymbol{L})^T}{K_P + (\boldsymbol{D}^e \boldsymbol{R})^T \boldsymbol{L}}\right].$$ *Eq. A-17*

B: Expansion of the memory surface

By definition, during virgin loading conditions, the yield surface persist tangent to the memory surface starting from a situation in which the MS and YS coincide. The memory surface expands around a pivot point A, which is diametrically opposed to the current stress (that evolves).

To derive the relationship between the kinematic and isotropic hardening of the memory, the consistency condition is enforced in the fixed pivot stress point, A. Recalling the MS equation:

$$f^M = \sqrt{(\boldsymbol{s} - p\boldsymbol{\alpha^M}):(\boldsymbol{s} - p\boldsymbol{\alpha^M})} - \sqrt{2/3}\ p\ m^M = 0 \qquad \text{Eq. B-18}$$

The consistency condition is

$$\frac{df^M}{d\boldsymbol{\sigma}} d\boldsymbol{\sigma} + \frac{df^M}{d\boldsymbol{\alpha^M}} d\boldsymbol{\alpha^M} + \frac{df^M}{dm^M} dm^M = 0 \qquad \text{Eq. B-19}$$

Considering that in A: $d\boldsymbol{\sigma_A} = 0$, the first term in the previous equation is 0 and the consistency condition results in:

$$\frac{-p(\boldsymbol{s} - p\boldsymbol{\alpha^M})}{\sqrt{(\boldsymbol{s} - p\boldsymbol{\alpha^M}):(\boldsymbol{s} - p\boldsymbol{\alpha^M})}} d\boldsymbol{\alpha^M} + \sqrt{2/3}\, p\ dm^M = \qquad \text{Eq. B-20}$$

Considering also that A is diametrically opposite to $\boldsymbol{\sigma}$, it results that

$$\frac{(\boldsymbol{s_A} - p\boldsymbol{\alpha^M})}{\sqrt{(\boldsymbol{s_A} - p\boldsymbol{\alpha^M}):(\boldsymbol{s_A} - p\boldsymbol{\alpha^M})}} = -\boldsymbol{n} \qquad \text{Eq. B-21}$$

Which substituted in the 8-21 leads to

$$p\boldsymbol{n}\ d\boldsymbol{\alpha^M} + \sqrt{2/3}\, p\ dm^M = 0 \qquad \text{Eq. B-22}$$

$$dm^M = \sqrt{3/2}\,\boldsymbol{n}\ d\boldsymbol{\alpha^M} \qquad \text{Eq. B-23}$$

C: Translation of the memory surface

Liu et al. (2019) postulate that during virgin loading conditions (when the surfaces are tangent in $\boldsymbol{r} = \boldsymbol{r^M}$ or $\boldsymbol{\alpha} = \boldsymbol{r}_\alpha^M$) the amplitude of the plastic strains can be indifferently computed using the yield or the memory function,

$$\frac{|\dot{\boldsymbol{\varepsilon}}^{pl}|}{|\boldsymbol{R}|} = \langle L \rangle = \langle L^M \rangle \qquad \text{Eq. C-24}$$

As shown in Eq. C-24, the hypothesis leads to $\langle L \rangle = \langle L^M \rangle$. Considering the definition of the plastic multiplier (or loading index), the same equation leads to

$$\langle L \rangle = \frac{1}{K_p} \frac{\partial f}{\partial \boldsymbol{\sigma}}\bigg|_{\boldsymbol{\sigma^M}} : d\boldsymbol{\sigma}|_{\boldsymbol{\sigma^M}} = \frac{1}{K_p^M} \frac{\partial f}{\partial \boldsymbol{\sigma}}\bigg|_{\boldsymbol{\sigma^M}} : d\boldsymbol{\sigma}|_{\boldsymbol{\sigma^M}} \qquad \text{Eq. C-25}$$

When the condition $\langle L \rangle = \langle L^M \rangle$ is postulated, also $K_p = K_p^M$ holds (from Eq. C-24,).

By enforcing the consistency condition for the memory (at the tangent point with the YS), it results that

$$\frac{\partial f}{\partial \boldsymbol{\sigma}}\bigg|_{\boldsymbol{\sigma^M}} : d\boldsymbol{\sigma}|_{\boldsymbol{\sigma^M}} = -\frac{df^M}{d\boldsymbol{\alpha}^M} : d\boldsymbol{\alpha}^M - \frac{df^M}{dm^M} dm^M \qquad \text{Eq. C-26}$$

After substituting the Eq. C-25 in the Eq. C-26, and considering the MS equation (Eq. 2-14), it is obtained that

$$\langle L \rangle K_p^M = p\boldsymbol{n} : d\boldsymbol{\alpha}^M - \sqrt{\frac{2}{3}} p \, dm^M \qquad \text{Eq. C-27}$$

By substituting the equation of $d\boldsymbol{\alpha^M}$

$$K_p^M = p \, \frac{2}{3} \left[h^M \big(\boldsymbol{\alpha}_\theta^b - \boldsymbol{r}_\alpha^M \big) : \boldsymbol{n} - \frac{\mathbf{1}}{\langle L \rangle} \sqrt{\frac{3}{2}} \, dm^M \right] \qquad \text{Eq. C-28}$$

Considering that the during virgin loading conditions $\boldsymbol{r} = \boldsymbol{r}^M$ $\boldsymbol{\alpha} = \boldsymbol{r}_\alpha^M$ and that the exponential term in the expression of h is equal to 1, the plastic modulus K_p (Eq. 2-17), can be rewritten as

$$K_p = p \, \frac{2}{3} \frac{b_0}{(\boldsymbol{r}_\alpha^M - \boldsymbol{\alpha}_{ini}) : \boldsymbol{n} + C_\varepsilon} \big(\boldsymbol{\alpha}_\theta^b - \boldsymbol{r}_\alpha^M \big) : \boldsymbol{n} \qquad \text{Eq. C-29}$$

Equating the previous equation of K_p with $\tilde{h} = \frac{2}{3} \frac{b_0}{(\boldsymbol{r}_\alpha^M - \boldsymbol{\alpha}_{ini}) : \boldsymbol{n}}$ and K_p^M

$$\tilde{h} \big(\boldsymbol{\alpha}_\theta^b - \boldsymbol{r}_\alpha^M \big) : \boldsymbol{n} = h^M \big(\boldsymbol{\alpha}_\theta^b - \boldsymbol{r}_\alpha^M \big) : \boldsymbol{n} - \frac{\mathbf{1}}{\langle L \rangle} \sqrt{\frac{3}{2}} \, dm^M \qquad \text{Eq. C-30}$$

Considering also the definition of dm^M (and $\tilde{h}$), the MS hardening coefficient results in:

$$h^M = \frac{1}{2} \left[\frac{b_0}{(\boldsymbol{r}_\alpha^M - \boldsymbol{\alpha}_{ini}) : \boldsymbol{n} + C_\varepsilon} + \sqrt{\frac{3}{2}} \frac{m^M f_{shr} \langle -D \rangle}{\zeta \big(\boldsymbol{\alpha}_\theta^b - \boldsymbol{r}_\alpha^M \big) : \boldsymbol{n}} \right] \qquad \text{Eq. C-31}$$